JGR Oceans

Sensitivity of the Global Ocean Carbon Sink to the Ocean Skin in a Climate Model

Hugo Bellenger[1], Laurent Bopp[1], Christian Ethé[2], David Ho[3], Jean Philippe Duvel[1], Simona Flavoni[4], Lionel Guez[1], Takahito Kataoka[5], Xavier Perrot[1], Laetitia Parc[1], and Michio Watanabe[5]

[1]LMD/IPSL, ENS, Université PSL, École Polytechnique, Institut Polytechnique de Paris, Sorbonne Université, CNRS, Paris, France, [2]Institut Pierre Simon Laplace, CNRS, Paris, France, [3]Department of Oceanography, University of Hawai'i at Mānoa, Honolulu, HI, USA, [4]LIttoral ENvironnement et Sociétés, La Rochelle, France, [5]Japan Agency for Marine-Earth Science and Technology, Yokohama, Japan

Abstract The ocean skin is composed of thin interfacial microlayers of temperature and mass of less than 1 mm where heat and chemical exchanges are controlled by molecular diffusion. It is characterized by a cooling of ∼−0.2 K and an increase in salinity of ∼0.1 g/kg (absolute salinity) relative to the water below. A surface observation-based air-sea CO_2 flux estimate considering the variation of the CO_2 concentration in these microlayers has been shown to lead to an increase in the global ocean sink of the anthropogenic CO_2 by +0.4 PgC yr^{-1} (15% of the global sink). This study analyzes this effect in more details using a 15-year (2000–2014) simulation from an Earth System Model (ESM) that incorporates a physical representation of the ocean surface layers (diurnal warm layer and rain lenses) and microlayers. Results show that considering the microlayers increases the simulated global ocean carbon sink by +0.26 to +0.37 PgC yr^{-1} depending on assumptions on the chemical equilibrium. This is indeed about 15% of the global sink (2.04 PgC yr^{-1}) simulated by the ESM. However, enabling the ocean skin adjustment to feedback on ocean carbon concentrations reduces this increase to only +0.13 (±0.09) PgC y^{-1}. Coupled models underestimate the ocean carbon sink by ∼5% if the ocean skin effect is not included.

Plain Language Summary The ocean skin is a thin layer of less than a millimeter that is in contact with the atmosphere, where the heat and chemical exchanges are controlled by molecular diffusion. It typically corresponds to a temperature at the ocean interface that is cooler by −0.2 K than the water at a depth of a millimeter. It also corresponds to a salinity that is slightly higher at the interface. Taking into account these temperature and salinity changes in this thin layer can change calculations of the global ocean carbon sink substantially. We use a global Earth System Model including a representation of the ocean skin to study this impact. We found an increase of 15% in the simulated global ocean carbon sink. This is consistent with past studies. Enabling the flux to feedback on the ocean carbon concentration significantly reduces its impact. We conclude by discussing the uncertainties in the global ocean carbon sink associated with the formulation of the carbon flux and the representation of the ocean skin.

1. Introduction

The global ocean represents a major sink of anthropogenic carbon emissions, averaging 2.8 ± 0.4 PgC yr^{-1} during the decade 2011–2020 (26% of total CO_2 emissions, Friedlingstein et al., 2022). This estimate is obtained by using independent approaches: (a) An ensemble of global ocean biogeochemical models forced by atmospheric reanalysis and atmospheric CO_2 concentration and (b) an ensemble of observation-based data products using the Surface Ocean CO_2 Atlas (SOCAT, Bakker et al., 2016). These data are based on interpolations of oceanic CO_2 fugacity measurements, and then corrected for the preindustrial natural carbon outgassing (Regnier et al., 2022). These model- and data-based estimates, cumulated in time, are compared to estimates of changes in ocean carbon inventories based on hydrographic campaign (Gruber et al., 2019). Both approaches (a) and (b) have inherent uncertainties due to, for example, sparse coverage of oceanic CO_2 measurements (e.g., Olivier et al., 2022; Walker Brown et al., 2015) or the representation of unresolved processes in the numerical models. However, even a perfect agreement between these complementary approaches would hide uncertainties due to the consideration of oceanic variables (e.g., temperature, salinity, dissolved carbon concentrations) at a depth of one to several meters and not at the ocean interface. In situ CO_2 fugacity (or effective partial pressure) measurements are from

ships and to a lesser extent from moorings, both of which typically measure water characteristics at 1–5 m depth. In models, temperature (T), salinity (S) and the CO_2 partial pressure computed from alkalinity (Alk) and dissolved inorganic carbon (*DIC*) are mean values from the model's upper level that is typically 1–2 m but can be of 10 m in some Earth System Model (ESM) configurations. Yet, there can be substantial changes in *T, S,* Alk, and DIC within the first tens of centimeters (e.g., Ho & Schanze, 2020).

Under the stabilizing effect of solar radiation or rain, a thin stratification of a few tenths of meters to a few meters can form at the ocean interface. Diurnal warm layers correspond to a temperature increase near the ocean surface during daylight when the wind is weak and sky is clear (e.g., Soloviev & Lukas, 2014; Stommel et al., 1969). They are particularly frequent in the tropics but can also be strong and frequent in high latitudes during the summer (Bellenger & Duvel, 2009; Kawai & Wada, 2007; Stuart-Menteth et al., 2003). On the other hand, freshening by rain can lead to the formation of stable fresh and often colder lenses (e.g., Katsaros & Buettner, 1969; Moulin et al., 2021; Reverdin et al., 2012) that can correspond to a decrease down to −9 g/kg and −1.5 K (Reverdin et al., 2020). Rain lenses are frequent in the tropics where the precipitation rate is high and the wind speed is low (e.g., Drushka et al., 2016; Moulin et al., 2021) but they can also occur at higher latitudes (Supply et al., 2020; Ten Doeschate et al., 2019). In addition, vertical gradients in temperature and salinity exist in the viscous boundary microlayer that typically extends within the first millimeter of the ocean and constitutes the Temperature Boundary Layer (TBL) and the Mass Boundary Layer (MBL), which are the diffusive microlayers for temperature and salinity respectively (Figure 1). Saunders (1967) first described the physics of these layers in which the temperature and salinity gradients are controlled by sensible and latent heat fluxes and infrared radiation at the interface and by molecular and turbulent diffusion in the ocean. Most of the time, this leads to a cool skin of around −0.2 K to −0.3 K (Fairall et al., 1996) and to an increase in salinity of about 0.1 g/kg (Yu, 2010; Zhang & Cai, 2007; Zhang & Zhang, 2012), but the ocean skin can lead to cooler and fresher microlayers under rain conditions (Schlüssel et al., 1997; Soloviev & Lukas, 2014).

It has been suggested that thermohaline stratification in the first meters of the ocean impacts CO_2 exchange at the ocean interface. Diurnal warming tends to increase ocean outgassing (Ward et al., 2004). On the contrary, rain has been shown to have multiple effects such as increasing the gas transfer velocity either in or out of the ocean by enhancing near-surface turbulence and bubbles (Ho et al., 1997), increasing the carbon sink through dilution in the first meter of the ocean (Ho & Schanze, 2020; Turk et al., 2020). Note that freshening by sea-ice melt and river runoff in coastal regions can also impact near surface stratification and thus CO_2 fluxes by lowering the water-side CO_2 concentration (e.g., Dong et al., 2021; Miller et al., 2019), but these processes will not be examined in this study.

Air-sea CO_2 exchange occurs in the ubiquitous microlayer described above (e.g., Liss & Slater, 1974), and the temperature change across it has been suggested to be important. Robertson and Watson (1992) first suggested that the cool skin increases the global ocean carbon sink by +0.6 PgC yr-1 (positive flux downward) at atmospheric pCO₂ of 350 μatm. This estimate was then revised to +0.4 PgC yr^{-1} by taking into account sub-monthly wind variability (Van Scoy et al., 1995). Woods et al. (2014) showed that this estimate is dependent on the simplified formula used to diagnose the temperature difference across the microlayer and suggested that the previous estimates are overestimated. There has been some debate about whether one should consider the gross cool skin effect in the computation of the CO_2 fluxes as is the case in the above-cited studies. Indeed, as discussed in Bolin (1960), diffusion across the ocean Mass Boundary Layer (MBL) is the process that limits the rate at which CO_2 is exchanged between the atmosphere and the ocean. Due to the higher water molecular diffusion rate for heat than for mass (e.g., Saunders, 1967), the MBL is only a fraction of the TBL. From this, McGillis and Wanninkhof (2006) argued that the cool skin adjustment on CO_2 flux depends on the temperature difference across the MBL. Because this difference is a fraction of the total cool skin, they predict a weak CO_2 flux adjustment assuming a linear temperature profile in the TBL. Based on these considerations, Zhang and Cai (2007) estimated that the cool skin effect on CO_2 flux is about +0.05 PgC yr^{-1} and largely compensated by the increase in salinity in the MBL. However, they only consider the change in solubility associated with changes in temperature and salinity and not on the interfacial CO_2 concentration (see the discussion in Woolf et al. (2016)). Using a uniform −0.14 K temperature and a +0.1 g/kg salinity difference between the sub-skin and the interface, Woolf et al. (2016) estimate an increase of global ocean sink to be roughly +0.34 Pg C yr^{-1}. Using SOCAT-based product, and taking constant temperature and salinity differences in the ocean skin of −0.17 K and 0.1 g/kg, Watson et al. (2020) found a mean increase of ocean sink of +0.4 Pg C yr^{-1} for 1992–2018. Using monthly mean surface meteorology from
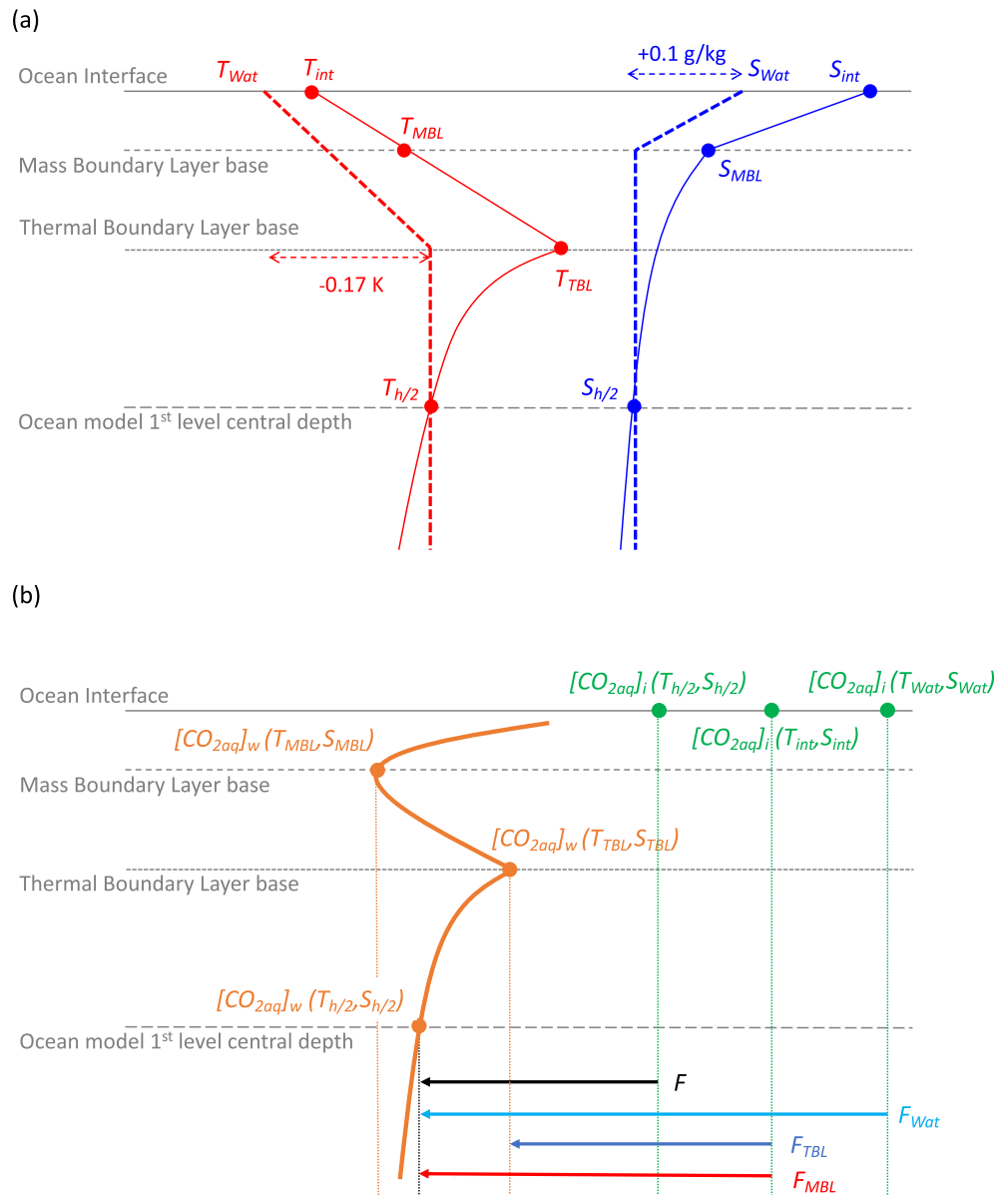
Figure 1. Schematic of (a) temperature (red) and salinity (blue) profiles below the ocean-atmosphere interface and within the first level of the ocean model of depth $h = 1$ m (central depth $h/2 = 0.5$ m) for a typical daylight situation and (b) water CO_2 concentration profile ($[CO_{2aq}]_w$, orange) and interfacial CO_2 concentrations ($[CO_{2aq}]_i$, green) corresponding to T and S taken at different depth from (a). Starting from the ocean interface, there is an increase in temperature with increasing depth down to the base of the Thermal Boundary Layer (TBL). This is the ocean's "cool skin". Then the temperature decreases with depth within the first meter due to a warm layer formation (in this case, the diurnal warming is less than the cool skin effect). There is a decrease with increasing depth for salinity, mostly within the Mass Boundary Layer (MBL) due to surface evaporation at the interface. The characteristics of the TBL and the MBL reflect the characteristics of molecular diffusion. Because species or mass diffusion is weaker than heat diffusion, the TBL is thicker than the MBL. The TBL is typically 0.5–1 mm thick and the MBL is typically 1/10th of TBL (1/5th in our simulation). A linear profile in temperature is assumed in the TBL to deduce T_{MBL} (see text for details). Dashed profiles represent the constant corrections that are applied to $T_{h/2}$ and $S_{h/2}$ to obtain T_{Wat} and S_{Wat} following Watson et al. (2020). Color arrows in (b) represent a subset of CO_2 fluxes from table 1 corresponding to T and S profiles from (a). $[CO_{2aq}]_i$ is mainly a decreasing function of T whereas $[CO_{2aq}]_w$ is an increasing function of T and S (see Appendix A). The black arrow represents the classical bulk flux (F), the red arrow represents the flux computed using the "equilibrium model" assumption (F_{MBL}), the blue arrows represent the flux using the "rapid model" assumption with an interactive ocean skin (F_{TBL}, blue) or a uniform one (F_{Wat}, light blue).

Table 1
Simulations and CO_2 Fluxes Calculation Details and Overall Results

Simulation	CO_2 fluxes	$[CO_{2aq}]_i = K_0 pCO_2^{atm}$	$[CO_{2aq}]_w$	Global CO_2 sink (Pg C yr^{-1})	CO_2 sink increase (Pg C yr^{-1})
DIAG	**F (prognostic)**	$T_{h/2}, S_{h/2}$	$T_{h/2}, S_{h/2}$	+2.04 (0.09)	–
	F_{MBL} (*diagnostic*)	T_{int}, S_{int}	T_{MBL}, S_{MBL}	+2.42 (0.09)	+0.37 (7.10^{-3})
	F_{TBL} (*diagnostic*)	T_{int}, S_{int}	$T_{TBL}, S_{TBL} = S_{MBL}$	+2.31 (0.09)	+0.26 (5.10^{-3})
	F_{Wat} (*diagnostic*)	$T_{h/2} - 0.17, S_{h/2} + 0.1$	$T_{h/2}, S_{h/2}$	+2.38 (0.1)	+0.33 (8.10^{-3})
	F_{skinM} (*diagnostic*)	$T_{h/2} + T_{int} - T_{TBL}$ $S_{h/2} + S_{int} - S_{MBL}$	$T_{h/2} + T_{MBL} - T_{TBL}$ $S_{h/2}$	+2.44 (0.09)	+0.39 (8.10^{-3})
	F_{skinT} (*diagnostic*)	$T_{h/2} + T_{int} - T_{TBL}$ $S_{h/2} + S_{int} - S_{MBL}$	$T_{h/2}, S_{h/2}$	+2.33 (0.09)	+0.28 (5.10^{-3})
	F_{noS} (*diagnostic*)	T_{int}, S_{MBL}	T_{MBL}, S_{MBL}	+2.44 (0.09)	+0.39 (8.10^{-3})
CPL	**F_{MBL} (prognostic)**	T_{int}, S_{int}	T_{MBL}, S_{MBL}	+2.18 (0.1)	+0.13 (0.09)

Note. This table gathers information on the two simulations that are presented in this study and the details of the different CO_2 prognostic fluxes used interactively to compute the carbon cycle in the model. The other fluxes are only diagnostic. Temperature and salinity that are used to compute the different terms of the CO_2 fluxes are reported. The subscripts correspond to the level at which the temperature and salinity are considered (see Figure 1a). The table also provides for the different fluxes the mean values of 2000–2014 annual global carbon sink (Pg C yr^{-1}, second last column) and of the difference compared to the basic flux F (last column), the corresponding year-to-year standard deviations are provided in parenthesis (no detrending applied).

ERA5 to compute the cool skin effect from Fairall et al. (1996), Dong et al. (2022) also found a comparable increase due to the cool skin effect of about 0.39 Pg C yr^{-1} for 1982–2020 without taking into account the competing MBL salinity gradient effect.

Note that, according to Watson et al. (2020), another correction has to be made to the SOCAT data because the measured CO_2 concentrations correspond to a depth of 1 m or more. They used satellite sub-skin temperature estimates (Banzon et al., 2016) to determine the waterside CO_2 concentration and found an additional increase in the flux of +0.4 PgC yr^{-1} for 1992–2018. Note that the Watson et al. (2020) estimate in the latest global carbon budget (Friedlingstein et al., 2022) used a new version of the SST satellite product (OISSTv2.1, Merchant et al., 2019) that corrected a cool bias present in the former version of this SST product (OISSTv2.0), but it remains an outlier among the other estimates. Using buoy SST as reference, Dong et al. (2022) found a warm bias in SOCAT SST which impact is +0.19 PgC yr^{-1} on the average for 1982–2020. Acknowledging the remaining substantial uncertainty around the river flux adjustment, the CO_2 sink increases due to the taking into account of the cool skin and warm bias correction appears to be able to reconcile the SOCAT-based estimates with the independent Gruber et al. (2019) 1994–2007 ocean sink estimate (Dong et al., 2022; Watson et al., 2020).

Previous evaluations of the impact of the diffusive microlayer on carbon exchanges were off-line diagnostics based on observations with limitations in terms of spatiotemporal coverage (Dong et al., 2022; Robertson & Watson, 1992; Shutler et al., 2020; Van Scoy et al., 1995; Watson et al., 2020; Woods et al., 2014; Woolf et al., 2016; Zhang & Cai, 2007). Furthermore, some of the studies used monthly-averaged of surface winds or idealized wind distributions to compute the CO_2 transfer velocity and most assumed constant and homogeneous temperature and salinity differences across the diffusive layers. To overcome the issue of diverse and limited data in time and space to compute global air-sea CO_2 fluxes, we use the coherent, although imperfect, set of variables from a coupled climate model (IPSL-CM6, Boucher et al., 2020). Further, to assess the necessity of taking into account the near-surface vertical gradients in ocean temperature and salinity, the Bellenger et al. (2017) parameterization that represents the near ocean surface temperature and salinity profiles (in the microlayer and below) that are not resolved by the ocean model is included in IPSL-CM6. Air-sea CO_2 fluxes are then diagnosed using a range of expressions from past literature to illustrate the necessity of a physically based and interactive diagnostic of the ocean surface layers in computing these fluxes.

The next section presents the design of the sensitivity experiments and the analysis tool used in this study, Section 3 contains the main results, and Section 4 discusses the uncertainties.

2. Approach and Methods

2.1. Earth System Model

The Institut Pierre-Simon Laplace Coupled Model Version 6.1, Low Resolution (IPSL-CM6A-LR) was used in this study, and details of the model and its evaluation can be found in Boucher et al. (2020). IPSL-CM6A-LR will be referred to as IPSL-CM6 in the following. Here, we only describe the model components and parameterizations that are important for our study. The atmospheric (LMDZ, Hourdin et al., 2019) and oceanic (NEMO, Madec et al., 2017) components exchange energy, water and carbon and are coupled every 90 min. The atmospheric model configuration has a horizontal resolution of $2.5° \times 1.5°$ and the ocean resolution is $1° \times 1°$. The ocean model configuration has a non-uniform vertical resolution that increases from 1 m at the surface to 10 m at 100 m depth and 200 m at the bottom. The ocean model includes the biogeochemical model NEMO-PISCES (Aumont et al., 2015), representing, in particular, the ocean carbon cycle and including both its inorganic and organic parts and their respective influences on the seawater concentrations of dissolved inorganic carbon (DIC) and alkalinity (Alk). The model salinity is absolute salinity in g/kg and so are the results presented here.

2.2. The Ocean Skin Parameterization

Figure 1a schematically represents the vertical temperature and salinity profiles that occur within the ocean model first layer and that are parameterized following Bellenger et al. (2017) that is available online (see data availability section). Figure 1a also provides the notations for the different depths that will be considered in this study, namely at the interface (int subscript) at the base of the MBL and TBL (MBL and TBL subscripts), and at the middle of the ocean model first level ($h/2$ subscript, with h the depth of the ocean model first level).

The ocean skin parameterization from Bellenger et al. (2017) used here is based on Saunders (1967). It computes differences in temperature and salinity between the interface and the bases of the TBL and MBL (Figure 1a). The parameterization assumes that the TBL and MBL depth are proportional to each other and proportional to the kinematic viscosity divided by the water-side friction velocity. This friction velocity is a function of surface fluxes of heat, radiation and momentum. The dependence of the Saunders proportional parameter on the turbulence regime is taken into account following Fairall et al. (1996). In addition, the stabilizing (freshening) and increased turbulence due to rain are also taken into account as detailed in Schlüssel et al. (1997). From this, the differences in temperature and salinity across the TBL and MBL ($T_{Int} - T_{TBL}$ and $S_{Int} - S_{MBL}$) and the TBL and MBL depths (z_{TBL} and z_{MBL}) are computed at each time step (see implementation details below). Note that because thermal diffusivity is larger than the diffusivity of salt, z_{TBL} is larger than z_{MBL}. The temperature at the base of the MBL is deduced assuming a linear temperature profile within the TBL from z_{MBL} and z_{TBL}.

The Bellenger et al. (2017) parameterization further diagnoses the differences in temperature and salinity between the base of the TBL/MBL and the ocean model first level at $h/2$ depth (Figure 1a). This part of the parameterization is an extension of Zeng and Beljaars (2005) that was originally limited to represent temperature increase with diurnal warming. Bellenger et al. (2017) extended it to salinity variations to allow negative temperature anomalies associated with rain. The one-dimensional heat and salinity budgets are integrated between a given depth d and the base of the microlayer assuming a temperature profile of the form:

$$T_{TBL} - T(z) = \left[\frac{(z + z_{TBL})}{-d + z_{TBL}} \right]^{\nu} (T_{TBL} - T_d) \tag{1}$$

With z being the depth (negative), T_d is the mixed layer temperature corresponding to a $d = 3$ m depth, and ν is a shape parameter equal to 0.3 in Zeng and Beljaars (2005). A similar profile is used for salinity. This provides a time evolution of temperature and salinity difference below the microlayer depending on surface fluxes (heat and radiative fluxes, momentum flux and rainfall) and vertical mixing that is parameterized in the framework of the Monin-Obukhov similarity theory (Large et al., 1994) and is a function of the same surface fluxes. Note that changes in salinity and temperature due to sea-ice melt are not included in the Bellenger et al. (2017) parameterization.

Inputs of the Bellenger et al. (2017) ocean skin parameterization are therefore surface fluxes (heat, radiation, rain and momentum) that are computed by the atmospheric component of IPSL-CM6 at each physical time-step. Therefore, the ocean skin parameterization is implemented in the atmospheric component and $T_{Int} - T_{TBL}$

and $S_{Int} - S_{MBL}$ and $T_{TBL} - T_{h/2}$ and $S_{MBL} - S_{h/2}$ are computed online at each atmospheric physical time-step (15 min). Note that the interface temperature is used to compute the turbulent heat fluxes and the upward long-wave radiation from the ocean surface of the next timestep.

To validate the ocean surface temperature and salinity gradients produced by IPSL-CM6 with the Bellenger et al. (2017) parameterization, we compared the distributions of 90 min outputs of our model with outputs of the Bellenger et al. (2017) parameterization forced by hourly ERA5 fluxes (Hersbach et al., 2020). The results are presented in Section 3.1.

2.3. Air-Sea CO_2 Flux Formulations

The air-sea CO_2 flux (F, in mol m^{-2} s^{-1}, positive downward) can be written as (McGillis & Wanninkhof, 2006):

$$F = k_w \sqrt{660/Sc(T)} \left[[CO_{2aq}]_i (T, S) - [CO_{2aq}]_w (T, S, DIC, Alk) \right]$$

$$= k_w \sqrt{660/Sc(T)} \left[K_0(T, S) pCO_2^{atm}(T, S) - [CO_{2aq}]_w (T, S, DIC, Alk) \right] \quad (2)$$

where k_w is the gas transfer velocity (in m s^{-1}) depending on the surface wind following Ho et al. (2006) and Wanninkhof (2014), Sc is the Schmidt number, $[CO_{2aq}]_i$ and $[CO_{2aq}]_w$ are the interfacial and waterside aqueous CO_2 concentrations (in mol m^{-3}). The interfacial CO_2 concentration can be written as the product of K_0, the CO_2 aqueous-phase solubility coefficient (a function of temperature and salinity in mol m^{-3} atm^{-1}, Weiss, 1974), and pCO_2^{atm} the CO_2 partial pressure (in atm) at the atmosphere interface, which only depends on the water vapor saturation pressure that is a function of the interface temperature and salinity (McGillis & Wanninkhof, 2006). The aqueous carbon concentration $[CO_{2aq}]_w$ is computed by NEMO-PISCES (Aumont et al., 2015) from the MOCSY carbonate chemistry set of equations (Orr & Epitalon, 2015) and is a function of the T, S, Alk, and DIC. One question is to determine the depths at which T, S, Alk, and DIC should be evaluated in the terms of Equation 2. In the standard version of the IPSL-CM6, the air-sea carbon flux is estimated by Equation 2 using T, S, Alk, and DIC at $h/2$. This classical bulk flux calculation is simply noted F (black arrow in Figure 1b).

Figure 1b, illustrates how $[CO_{2aq}]_w$ and $[CO_{2aq}]_i$ vary with T and S taken at different depths for the situation depicted in Figure 1a. $[CO_{2aq}]_w$ is an increasing function first of S and then of T (see Appendix A and Woolf et al., 2016). Below the interface, $[CO_{2aq}]_w$ decreases with increasing depth due to the salinity increase in the MBL (Figure 1a). Below the MBL base and in the absence of rain, the changes in S are weak and changes in T control the changes in $[CO_{2aq}]_w$. Thus, $[CO_{2aq}]_w$ increases with depth and thus with temperature in the TBL; then, it decreases down to $h/2$-depth in relation to the diurnal warm layer (Figure 1a). On the other hand, $[CO_{2aq}]_i$ is a decreasing function first of temperature and then salinity (see Appendix A) and will depend on the depth at which temperature and salinity are evaluated. In the situation represented in Figure 1a, with $T_{h/2} > T_{int}$, this lead to $[CO_{2aq}]_i(T_{int}, S_{int}) > [CO_{2aq}]_i(T_{h/2}, S_{h/2})$ (Figure 1b).

The limiting step in CO_2 exchanges between the ocean and the atmosphere is the diffusion of CO_2 molecules in the MBL, which is the diffusive layer for salt (Bolin, 1960; McGillis & Wanninkhof, 2006). According to McGillis and Wanninkhof (2006), the flux should then be computed from the difference in CO_2 concentrations at the top (the interface) for $[CO_{2aq}]_i$ and at the bottom of this layer for $[CO_{2aq}]_w$. This flux is noted F_{MBL} (red arrow in Figure 1b).

As underlined by Woolf et al. (2016), this formulation implicitly hypothesizes a linear temperature profile and that the chemical equilibrium is reached in the MBL. They name this hypothesis the "equilibrium model." However, the residence time of a water parcel in the TBL is generally shorter than the timescale for chemical repartitioning of the carbonate species induced by changes in temperature and salinity, which is on the order of 10s (Dong et al., 2022; Woolf et al., 2016). Therefore, in what they name the "rapid model", Woolf et al. (2016) argue that the TBL base temperature and salinity (Figure 1a) account for the MBL chemical repartitioning better and should be used to compute $[CO_{2aq}]_w$. The flux computed accordingly to this "rapid model" is noted F_{TBL} (blue arrow in Figure 1b). As the TBL base temperature is warmer than the MBL base temperature (Figure 1a), the rapid model leads to a larger waterside CO_2 concentration than the equilibrium model (see Appendix A). Therefore, F_{TBL} leads to a weaker increase in CO_2 sink than F_{MBL} (Figure 1b).

To assess the impact of considering a uniform ocean skin (Watson et al., 2020), we introduce another diagnostic F_{Wat} (light blue arrow in Figure 1b) for which $[CO_{2aq}]_w$ is computed at $h/2$-depth and $[CO_{2aq}]_i$ is computed using empirically-based constant differences of -0.17 K and $+0.1$ g/kg across the TBL and the MBL respectively (see Figures 1a and 1b).

Table 1 synthesizes the different CO_2 fluxes that are computed and details the corresponding temperature and salinity that are considered. Additional diagnostics F_{SkinM} and F_{SkinT} are computed as F_{MBL} and F_{TBL} but neglecting T and S changes below the ocean skin. Comparing F_{SkinM} and F_{SkinT} results to F_{MBL} and F_{TBL} quantifies the impact of diurnal warm layers and rain lenses stratification within the first model layer of 1 m depth. A last diagnostic F_{NoS} is comparable to F_{MBL} but does not take into account the limiting effect of the salty skin.

All the CO_2 fluxes are computed online by the IPSL-CM6 model every 45 min, which corresponds to the ocean model timestep that considers the temperature and salinity corrections computed by Bellenger et al. (2017) during the latest coupling timestep (every 90 min). To evaluate Alk and DIC at a given depth for the computation of $[CO_{2aq}]_w$ in Equation 2, we assume that, near the surface, Alk and DIC differ from their value at $h/2$-depth only because of concentration changes caused by rain and evaporation. We thus assume that they have the same ratio of dilution as salinity and so we can write $\frac{S_{MBL}-S_{h/2}}{S_{h/2}} = \frac{Alk_{MBL}-Alk_{h/2}}{Alk_{h/2}} = \frac{DIC_{MBL}-DIC_{h/2}}{DIC_{h/2}}$.

Considering the other terms in Equation 2: We assume that the bulk transfer parameterization for k_w derived from the global ^{14}C budget (Wanninkhof, 2014), which is usually applied to atmospheric and oceanic parameters, corresponding typically to 10 m height and 5 m depth, can be used to evaluate the ocean skin effect on the carbon fluxes. The implications of this hypothesis will be further discussed in detail in the discussion section. Note that we do not include the rain effect on the transfer velocity (Ho et al., 1997). The Schmidt number is a function of temperature and salinity and should be evaluated below the ocean skin (Yang et al., 2022). However, evaluating it at the interface, at the MBL base or at the ocean model first level leads to very small differences (not shown). Therefore, in the following, it will always be evaluated at the ocean model first level ($T_{h/2}$ and $S_{h/2}$).

2.4. Simulations

Two 15-year IPSL-CM6 simulations with imposed global-mean atmospheric CO_2 concentration corresponding to present-day conditions (years 2000–2014) were performed. We repeated the last 15 years of the CMIP6 historical simulations with IPSL-CM6A-LR (scenario starts from 2015), using the r1i1p1f1 member available on ESGF as initial conditions for January 2000 (Boucher et al., 2020, link in the Data Availability Statement). Both simulations use the IPSL-CM6 model (CMIP6 version) with the Bellenger et al. (2017) parameterization included. In contrast with the CMIP6 version of the model, the Bellenger et al. (2017) parameterization was used to compute the sensible and latent heat and the infrared fluxes. In the diagnostic (DIAG) simulation, the prognostic CO_2 flux used to compute the evolution of the oceanic carbon was from the classical bulk formulation F and the CO_2 fluxes deduced from other formulations were calculated only as diagnostics (Table 1). In the coupled (CPL) simulation, the F_{MBL} carbon flux was used to compute the evolution of oceanic carbon so that the new parameterization affected the simulated ocean carbon cycle. Because the equilibrium model (F_{MBL}) leads to a larger adjustment than the rapid model (F_{TBL}), this will provide an upper limit of the impact of the ocean skin on CO_2 flux in a coupled framework. We indicate the considered simulation using a superscript on the CO_2 flux notation (e.g., F^{DIAG}).

3. Results

3.1. Air-Sea CO_2 Fluxes

Figure 2 compares CO_2 fluxes from the DIAG simulation to the SeaFlux data product of Fay et al. (2021). The mean CO_2 flux F^{DIAG} over 2000–2014 (Figure 2a) shows a latitudinal pattern consistent with SeaFlux (Figure 2b). Main outgassing regions are found in tropical and sub-tropical oceans with fluxes down to -30 g C m^{-2} yr^{-1} in the eastern Equatorial Pacific. The ocean acts mainly as a sink for subtropical and mid-latitude regions with maxima reaching $+40$ g C m^{-2} yr^{-1} locally in the Southern Ocean and in the storm track regions. There are some large local biases such as in the northern Pacific Ocean where the sink is overestimated by the model by up to $+20$ g C m^{-2} yr^{-1} and in the equatorial ocean where the outgassing is underestimated in a comparable manner (Figure 2c). Overall, the global oceanic CO_2 sink simulated by our
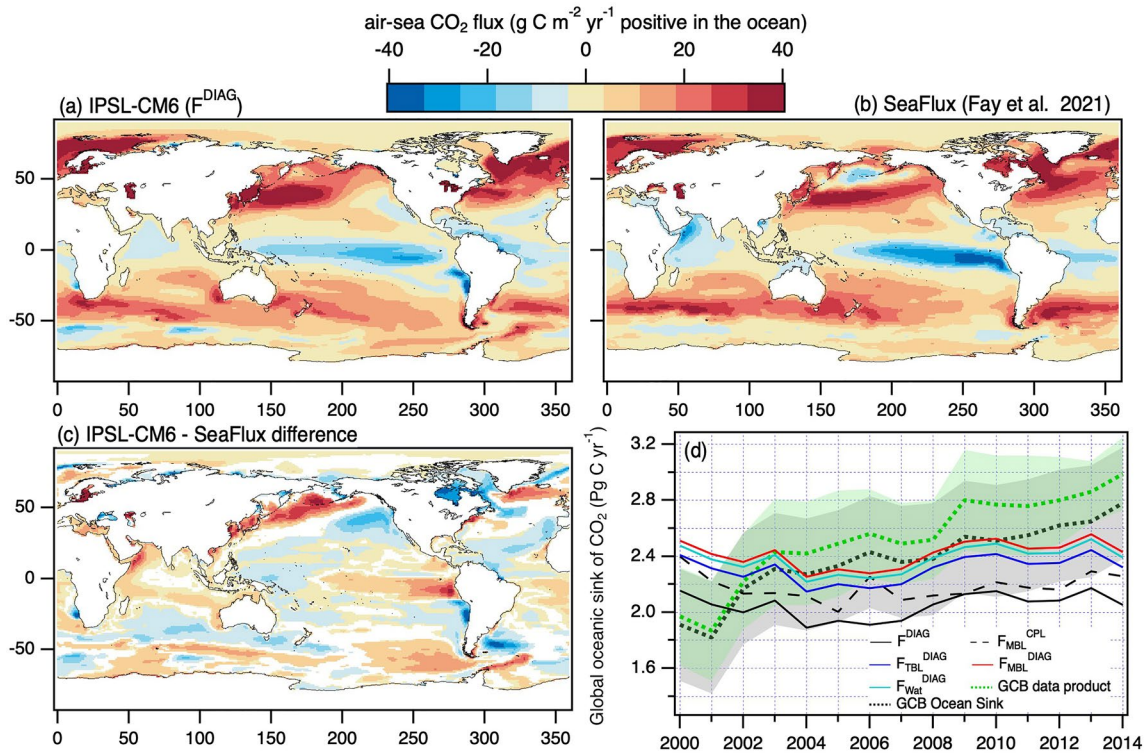
Figure 2. Maps of mean air-sea CO_2 fluxes between 2000 and 2014 (positive into the ocean, colors) from (a) the F^{DIAG} flux from the DIAG simulation with IPSL-CM6 and (b) SeaFlux data product average for the 6 interpolation methods for the pCO_2 maps and 5 wind products presented in Fay et al. (2021) and (c) the difference between IPSL-CM6 and SeaFlux product (only difference significant to the 99% level are plotted). (d) Time series of the global annual CO_2 sink (PgC yr^{-1}) from the Global Carbon Budget (Friedlingstein et al., 2022) based on data products (dashed green, standard deviation shaded), models and data products (dashed black, standard deviation shaded) and computed from F^{DIAG} (thin black), F_{MBL}^{DIAG} (thin red), F_{TBL}^{DIAG} (thin blue) and F_{Wat}^{DIAG} (thin light blue) IPSL-CM6 reference simulation (DIAG) and F_{MBL}^{CPL} (thin dashed black) from the coupled (CPL) simulation.

model in the DIAG simulation (Figure 2d black thin line) is underestimated compared to the Global Carbon Budget (GCB) estimate that includes both models and data products or only the latter (*resp.* bold dashed black and green lines, Friedlingstein et al., 2022). The CPL simulation only slightly reduces the underestimation of the global sink by the model (Figure 2d black thin dashed line). In addition, neither DIAG nor CPL actually reproduce the increasing tendency in the global oceanic sink (less than +0.01 PgC yr^{-1} vs. +0.06 PgC yr^{-1} for GCB during 2000–2014).

3.2. Near-Surface *T* and *S* Vertical Gradients

Figure 3 shows the distributions of temperature differences across the TBL, and salinity differences across the MBL and between the base of these layers and the oceanic mixed layer taken at 3 m. The values were obtained using the Bellenger et al. (2017) parameterization in IPSL-CM6 (solid lines) and the same parameterization forced by ERA5 (dashed lines). Note that, in our model, the temperature difference across the MBL is about 1/5th of the difference across the TBL. First, the distributions produced by IPSL-CM6 and diagnosed from ERA5 are in good agreement, except for slightly more frequent temperature differences below −0.4 K across the TBL in IPSL-CM6 (Figure 3a). The global mean differences in salinity and temperature across MBL and TBL are 0.06 g/kg and −0.23 K for IPSL-CM6 and 0.07 g/kg and −0.17 K for ERA5. These values are comparable with the values of 0.1 g/kg and −0.17 K chosen by Watson et al. (2020) based on in situ measurements by Donlon et al. (2002). Below the ocean skin, the change in temperature and salinity due to warm layers and rain lenses are generally an order of magnitude lower than changes in the ocean skin, with mean differences on the order of 10^{-2} K for temperature and 10^{-3} g/kg for salinity. Therefore, and as it will be shown in the next section and consistently with Woolf et al. (2016), the difference in the global ocean CO_2 sink due to near-surface *T* and *S* vertical gradients from Bellenger et al. (2017) is mainly due to the ocean skin.
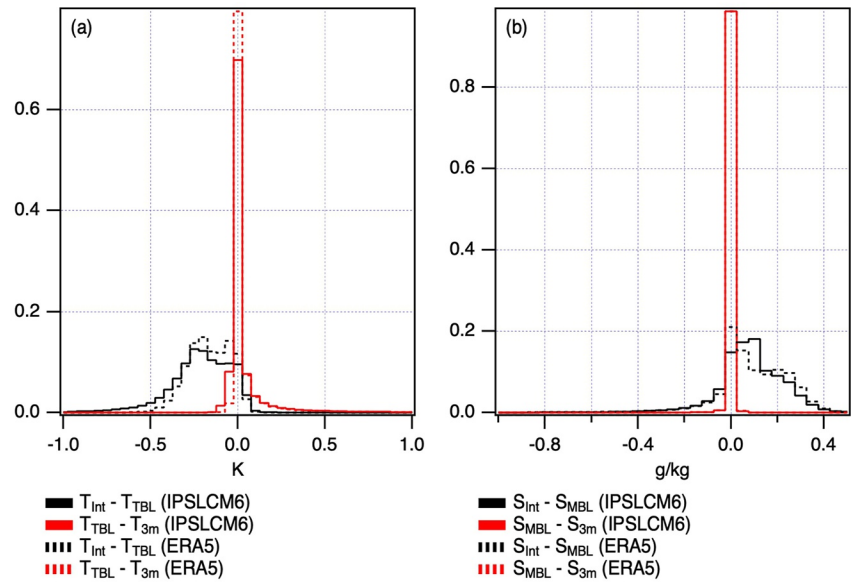
Figure 3. Probability distributions of (a) the temperature differences between the interface and the base of the Thermal Boundary Layer $T_{Int} - T_{TBL}$ (TBL, black) and the base of the TBL and $d = 3$ m depth $T_{TBL} - T_{3m}$ (red) and (b) likewise for salinity $S_{Int} - S_{MBL}$ (black) and $S_{MBL} - S_{3m}$ (red). Solid lines are from the 15 years DIAG simulation with IPSL-CM6 and dashed lines are from Bellenger et al. (2017) forced by 18 years of 1-hr ERA5 data.

Figure 4 shows the maps of mean temperature and salinity differences across their respective diffusive boundary layers (TBL and MBL) in IPSL-CM6 and ERA5. Spatial distributions of the cooling and increase in salinity in the TBL and MBL by IPSL-CM6 and ERA5 are in close agreement except for the high latitudes where the model is producing too strong a cooling (Figures 4a and 4b). There is no such overestimation in salinity increase across the MBL at high latitudes (Figures 4c and 4d). In fact, at high latitudes in the model, strong cooling of the sea surface by infrared radiation and sensible heat flux gives a stronger cool skin (around −0.4 K) that is not associated with a clear increase in salinity across the MBL. The difference in temperature across the TBL is stronger than the −0.17 K chosen by Watson et al. (2020) almost everywhere in the tropics and subtropics. A similar feature is visible for the change in salinity across the MBL (Figures 4c and 4d), which is frequently stronger than the 0.1 g/kg threshold in the tropical and subtropical regions except for the Intertropical Convergence Zone (ITCZ) region. In the ITCZ, frequent rain and light winds lead to a fresh ocean skin with $S_{Int} - S_{MBL} \sim -0.1$ g/kg and a cool skin of −0.3 K. In the subtropics, large evaporation and stronger wind speed may lead to large positive $S_{Int} - S_{MBL} \sim +0.3$ g/kg and a cool skin of −0.4 K. Finally, in the mid-latitudes, high wind speeds induce strong mixing that largely reduces the TBL and MBL effects.

3.3. Impacts on Air-Sea CO₂ Fluxes—Diagnostics

The annual mean global ocean carbon sinks, estimated from the DIAG simulation for the standard flux (F^{DIAG}), for the different diagnostics (F_{MBL}^{DIAG}, F_{TBL}^{DIAG}, F_{Wat}^{DIAG}, F_{SkinM}^{DIAG}, F_{SkinT}^{DIAG}, and F_{NoS}^{DIAG}) and the corresponding differences with F^{DIAG} are reported in Table 1. The increase in the global ocean carbon sink from the diagnosed fluxes ranges from +0.26 to +0.39 PgC yr⁻¹, which is 13%–19% of the standard sink of 2.04 PgC yr⁻¹.

In the following, we will focus on F_{MBL}^{DIAG}, F_{TBL}^{DIAG}, and F_{Wat}^{DIAG}, which are reported in Figure 5. First, the global sink computed from F_{MBL}^{DIAG} (+0.37 PgC yr⁻¹) increases more than the one computed from F_{TBL}^{CT} (+0.26 PgC yr⁻¹). This is because the former includes the effect of a large part of the cool skin on $[CO_{2aq}]_w$, which is an increasing function of T (Appendix A). The equilibrium model gives a sink strengthening 40% larger than with the rapid model. Using the rapid model but uniform ocean skin F_{Wat}^{DIAG} leads to stronger sink (+0.33 PgC yr⁻¹) than with the interactive ocean skin F_{TBL}^{DIAG} (+0.26 PgC yr⁻¹). The difference in the adjustments using F_{MBL}^{DIAG}, F_{TBL}^{DIAG}, and F_{Wat}^{DIAG} are statistically significant (to the 99.9% level, see the standard deviations in the last column of Table 1). The three flux estimates induce an additional sink that increases with time at a rate of +1.5 × 10⁻³ PgC yr⁻² (Figure 5b), which is comparable to the +2.5 × 10⁻³ PgC yr⁻² obtained by
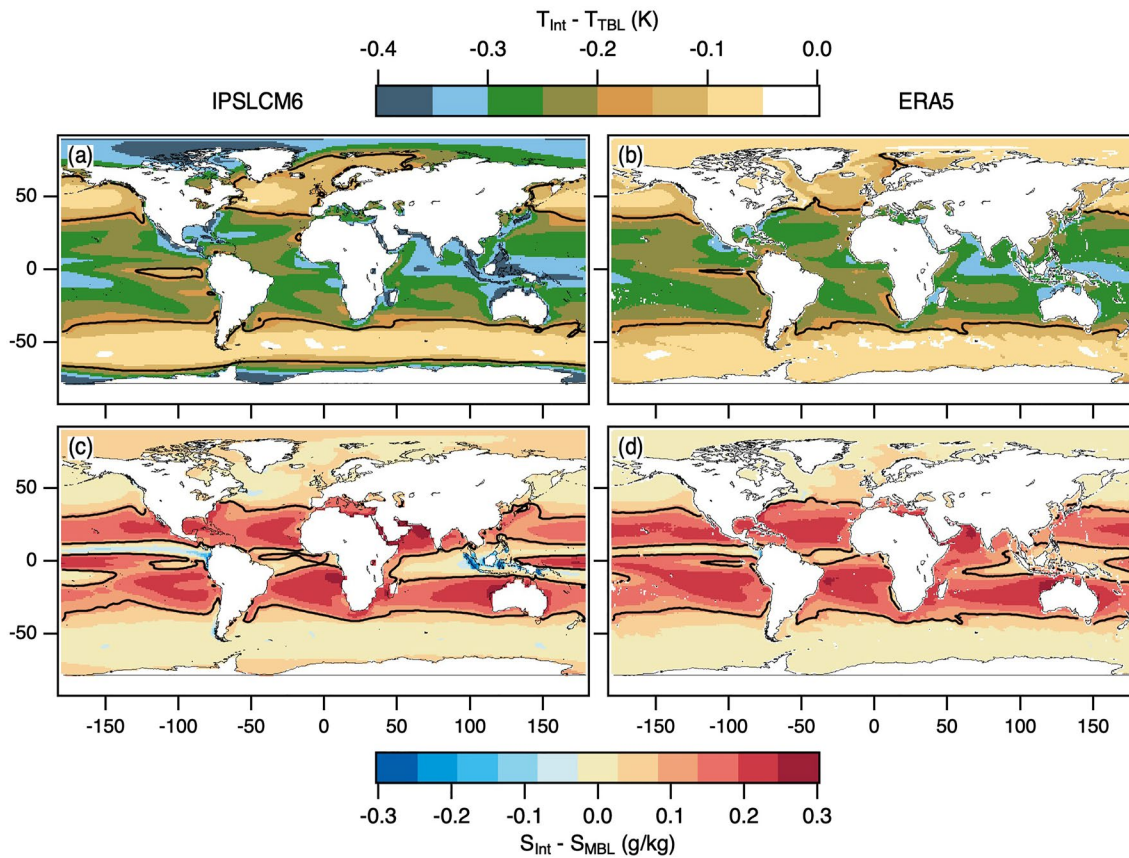
Figure 4. The mean difference in temperature (K) between the interface (T_{Int}) and the base of the Thermal Boundary Layer (T_{TBL}) for (a) the 15 years of DIAG simulation and (b) 18 years of ERA5; and mean difference in salinity (g/kg) between the interface (S_{Int}) and the base of the Mass Boundary Layer (S_{MBL}) for (c) the 15 years of DIAG simulation and (d) 18 years of ERA5. The black contours correspond to −0.17 K for (a and b) and +0.1 g/kg for (c and d).

Dong et al. (2022). Figure 5c shows the seasonal variations of hemispherical CO_2 sink with maxima during the corresponding hemisphere's winter. F_{Wat}^{DIAG} shows weaker seasonal variations than F_{MBL}^{DIAG} and F_{TBL}^{DIAG} in both hemispheres. In addition, the overestimation of the global sink when using a uniform ocean skin (F_{Wat}^{DIAG} vs. F_{TBL}^{DIAG}) is mainly due to an overestimation of the sink in the southern hemisphere. The hemispherical sinks variations largely compensate to result in a weak seasonal variation of the global sink.

Figure 6 compares F^{DIAG} to the three alternative estimates F_{MBL}^{DIAG}, F_{TBL}^{DIAG}, and F_{Wat}^{DIAG}. These estimates increase the ocean CO_2 sink everywhere with some specific patterns. F_{MBL}^{DIAG} increases CO_2 sink especially in the tropical and subtropical oceans (Figure 6b). This increase is particularly marked in the trade winds regions of the western Pacific and Atlantic Oceans and, for the mid-latitudes, in the Gulf Stream, the Kuroshio, and the Agulhas Current regions. Because the cool skin temperature difference is not a function of wind alone, there is no simple relationship between the flux adjustment in Figure 6b neither with the mean cool skin shown in Figure 4a nor with the wind speed as it is discussed in Section 4.3. However, regions of very large cool skin, like the warm pool and polar regions, correspond to weak flux adjustment because the strong cool skin are associated with very low wind speed. Although weaker, the adjustment using F_{TBL}^{DIAG} shows a comparable pattern (Figure 6c). In contrast, applying F_{Wat}^{DIAG} would increase CO_2 sink in the mid-to-high latitudes (40–70N and 40–70S, Figure 6d), especially in the Southern Ocean where F_{Wat}^{DIAG} would lead to an increase in air-sea carbon fluxes that exceed 10% of the mean annual carbon flux (Figure 6a). Mid-to-high latitudes regions are characterized by relatively high winds and intense near-surface turbulence that largely erodes the temperature gradient within the TBL to cooling weaker than −0.1 K (Figure 4a) and thus weaker than −0.17 K. Strong winds also increase the CO_2 flux by increasing the gas transfer velocity k_w in Equation 2. Therefore, in IPSL-CM6 and using the rapid model assumption, using a constant difference of −0.17 K following Watson et al. (2020) would result in an overestimate of the impact of the cool skin on CO_2 fluxes in mid-to-high latitudes (+1 to +2 g C m^{-2} yr^{-1}
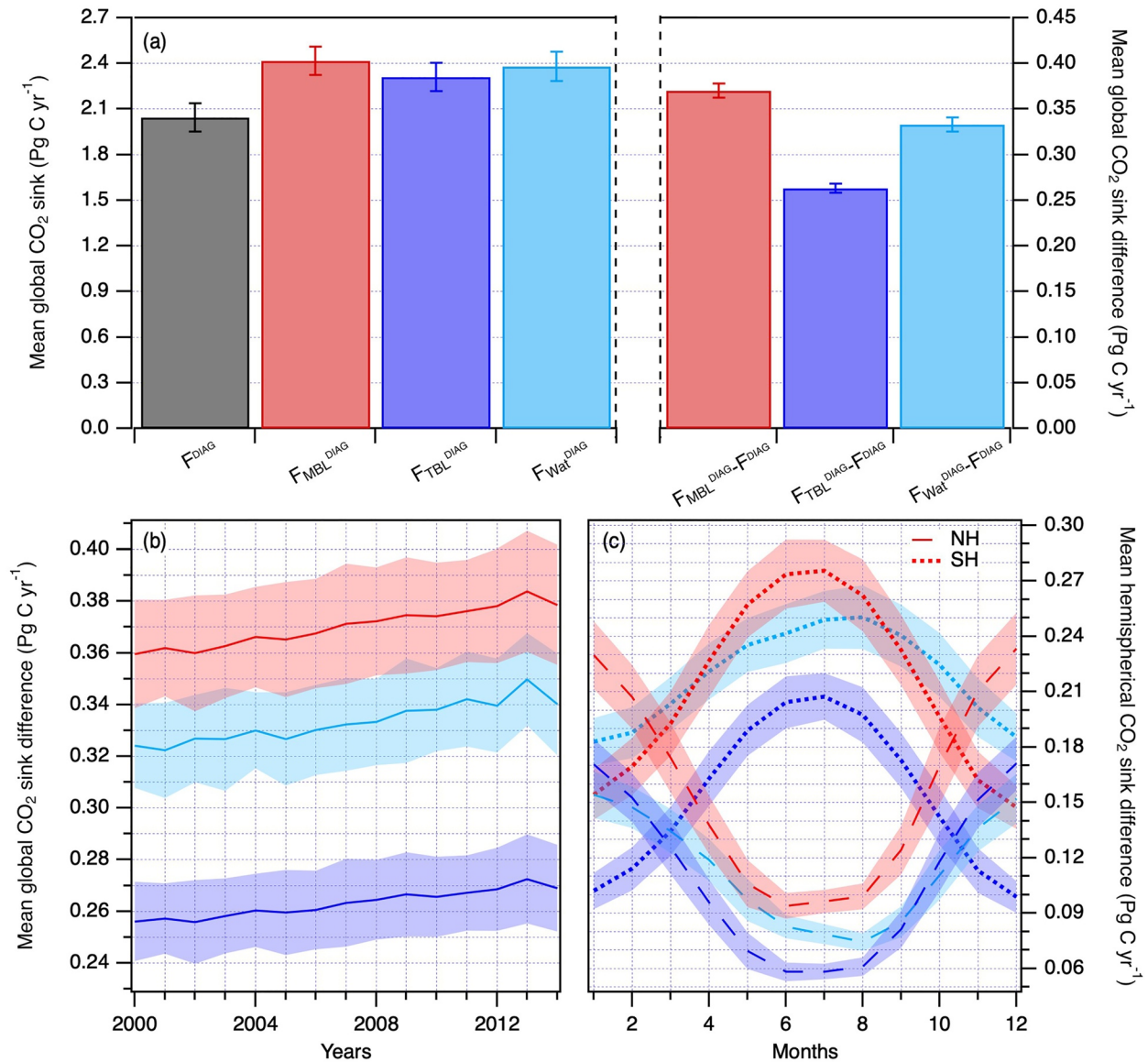
Figure 5. (a) Mean 2000–2014 global ocean carbon sink (PgC yr^{-1}, left axis) from DIAG simulation computed with F^{DIAG} (black bar), F_{MBL}^{DIAG} (red bar), F_{MBL}^{DIAG} (blue bar) and F_{Wat}^{DIAG} (light blue bar) and corresponding mean differences in global carbon sink with the one computed with F^{DIAG} (PgC yr^{-1}, right axis). Whiskers represent the year-to-year standard deviations (no detrending applied). (b) Time series of the annual global ocean CO_2 sink differences between F_{MBL}^{DIAG} (red), F_{TBL}^{DIAG} (blue) and F_{Wat}^{DIAG} (light blue) and F^{DIAG} from DIAG simulation (Pg yr^{-1}, shading are the intra-annual standard deviation of the corresponding differences) and (c) monthly mean seasonal cycle of the northern (dashed) and southern (dotted) hemisphere CO_2 sink differences (Pg yr^{-1}, colors are as in (b), shading represents the day-to-day standard deviation for each month).

in the Southern Ocean, Figures 6b and 6c), as well as on the global CO_2 sink (Table 1, +0.33 Pg C yr^{-1} for F_{Wat} vs. +0.26 Pg C yr^{-1} for F_{TBL}).

The spatial distribution of F^{DIAG} carbon flux shows a clear seasonality with a large carbon sink in the mid-to-high latitudes of the winter hemisphere where stronger winds blow (Figures 7a and 7b). Furthermore, Figure 7 c-f show the spatial pattern behind the hemispherical variation of the CO_2 sink of Figure 5c. F_{MBL}^{DIAG} and F_{TBL}^{DIAG} increase the CO_2 sink mainly in the winter hemisphere, with maxima in the subtropical Gulf Stream and Kuroshio regions in boreal winter (Figures 7c and 7e), with weak increase is observed in the tropical and subtropical regions of the summer hemisphere (Figures 7d and 7f). In contrast, F_{Wat}^{DIAG} shows seasonal variability that is stronger higher latitudes in the northern Atlantic and Pacific oceans in DJF and in the Southern Ocean in JJA (+2 to +3 g C m^{-2} yr^{-1}) (Figures 7g and 7h). The increase in CO_2 sink in the
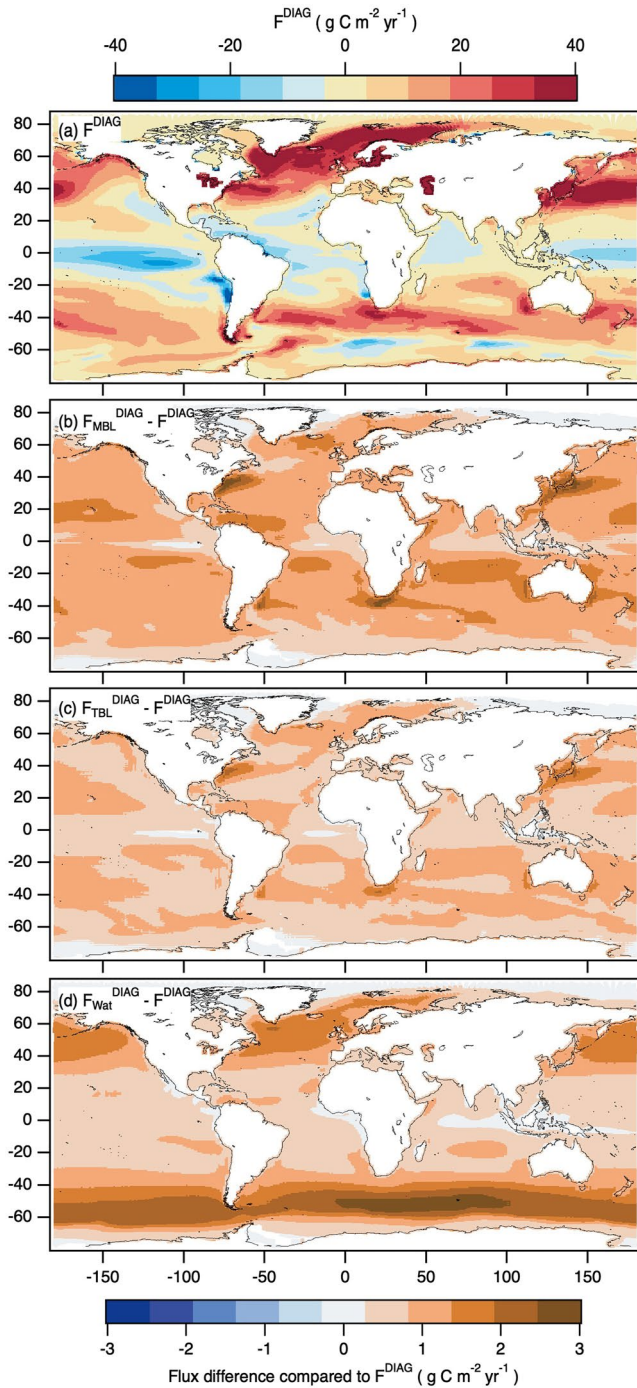
F^{DIAG} (g C m^{-2} yr^{-1})

Flux difference compared to F^{DIAG} (g C m^{-2} yr^{-1})

Figure 6. Mean maps for 15 years of DIAG simulation of (a) F^{DIAG} (g C m^{-2} yr^{-1}) and (b) the $F_{MBL}^{DIAG} - F^{DIAG}$ difference (g C m^{-2} yr^{-1}), (c) the $F_{TBL}^{DIAG} - F^{DIAG}$ difference (g C m^{-2} yr^{-1}) and (d) the $F_{Wat}^{DIAG} - F^{DIAG}$ difference (g C m^{-2} yr^{-1}). Only differences significant to the 99% level with the student t-test are plotted.

tropics does not show comparable equatorial asymmetry and the Southern Ocean adjustment remains a non-negligible part of the average carbon flux in DJF (+1 to +2 g C m^{-2} yr^{-1}) explaining the weaker seasonal variations in Figure 5c.

When comparing the increase in the carbon sink with (i.e., F_{MBL}^{DIAG} for the equilibrium model and F_{TBL}^{DIAG} for the rapid model) and without (i.e., F_{SkinM}^{DIAG} for the equilibrium model and F_{SkinT}^{DIAG} for the rapid model) taking into account the sub-skin temperature and salinity variations above $h/2$-depth shows that, as expected from Figure 3, the effect of unresolved warm layers and rain lenses is minimal for an ocean model with 1 m resolution at the surface, resulting in a reduction of the sink by only −0.02 PgC yr^{-1}. This difference is mainly due to warm layer formation in the equatorial oceans (not shown). In addition, comparing the F_{MBL}^{DIAG} and F_{NoS}^{DIAG} sinks shows that the compensating effect of the saline skin on the global CO_2 sink is also weak (−0.02 PgC yr^{-1}) and mainly located in tropical regions where $S_{int} - S_{MBL}$ is large (Figure 4c).

3.4. Impacts on Air-Sea CO_2 Fluxes—Prognostic

In the previous section, we showed the impact of the ocean skin on air-sea CO_2 fluxes diagnostics that do not impact the ocean carbon budget. In this section, we compare air-sea carbon fluxes from F^{DIAG} to those from a coupled (CPL) simulation in which F_{MBL}^{CPL} is used to compute the evolution of DIC in the ocean model. Because the associated feedback is clearly negative, an attenuated effect is to be expected. Figure 8a shows the 2000–2014 global ocean carbon sink in DIAG and CPL simulations using the respective prognostic fluxes F^{DIAG} and F_{MBL}^{CPL} as well as their difference (also in Table 1). In CPL, the ocean carbon sink is increased by about +0.13 (±0.09) Pg C yr^{-1} compared to DIAG (Figure 8a). This is only about 35% of the ocean sink augmentation diagnosed for F_{MBL}^{DIAG} (+0.37 ± 7 10^{-3} Pg C yr^{-1}). In addition, one can note that the year-to-year standard deviation of the $F_{MBL}^{CPL} - F_{blk}^{DIAG}$ resulting global ocean sink is large and about +0.09 Pg C yr^{-1}. This is comparable to the standard deviations of the global ocean sink diagnosed from either DIAG or CPL and larger than the year-to-year standard deviations of the adjustment diagnosed in DIAG. This is because using F_{MBL} instead of F as a prognostic carbon flux modifies the simulated marine biogeochemistry that feedbacks on the ocean heat budget through a biophysical coupling (Lengaigne et al., 2009) and on the simulated climate so that the DIAG and CPL simulations diverge. This divergence manifests itself through difference in patterns and timing of atmospheric dynamical synoptic perturbations in particular at mid-to-high latitudes. This results in larger differences in CO_2 flux variability in these regions (Figure 8b, the black curve and its standard deviation). Because of this divergence of the two simulations, we only show zonal mean profiles of the CO_2 flux and ocean model first level pCO$_2$ differences in Figure 8b (shadings represent their year-to-year variability). The use of F_{MBL}^{CPL} tends to increase the ocean carbon sink at almost all latitudes. This increase in CO_2 flux is only significant to the 95% confidence level. However, the increase in the first level of pCO$_2$ is significant in the tropics (Figure 8b, the red curve). There is an accumulation of carbon at the ocean surface in the CPL simulation. This can explain the limitation of the increase in the carbon sink when using F_{MBL} rather than F as prognostic flux. Therefore, taking into account all interaction loops and depending on the ability of the ocean model to transfer the carbon into the ocean interior, the use of F_{MBL} leads to a significantly weaker adjustment in a coupled framework than what could be inferred from a simple offline diagnostic.
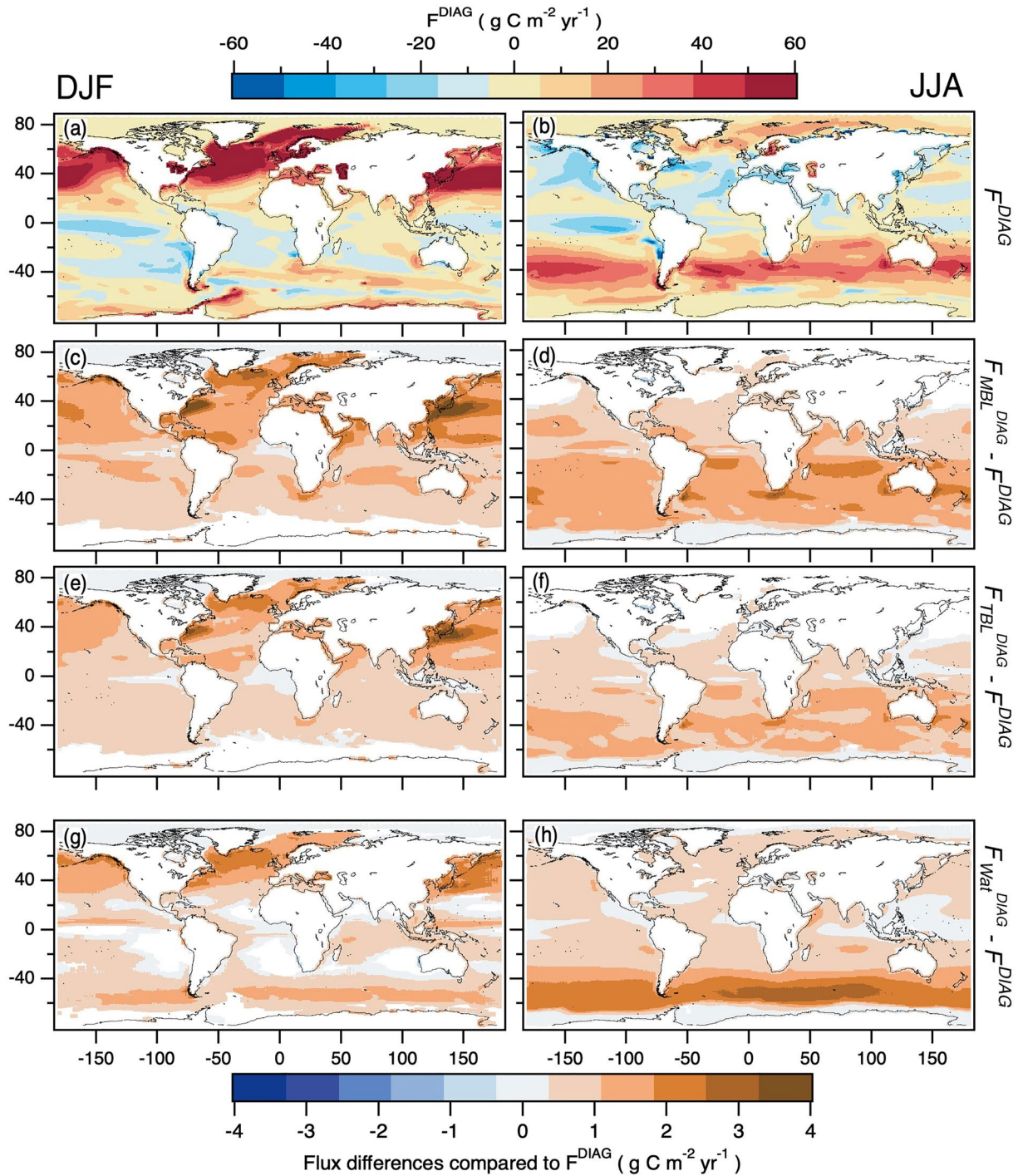
Figure 7. As Figure 5 but for December-January-February (a, c, e, and g) and June-July-August (b, d, f, and h). Only differences significant to the 99% level with the student *t*-test are plotted.

4. Discussion

4.1. Uncertainties Due To the Ocean Skin Representation

A first source of uncertainty is the representation of the ocean skin. Assuming a linear dependency of the CO_2 sink adjustment to the temperature difference in the TBL and using the mean difference of 0.06 K between IPSL-CM6 and ERA5 estimates lead to an uncertainty of ± 0.07 PgC yr^{-1}. Taking into account this uncertainty,
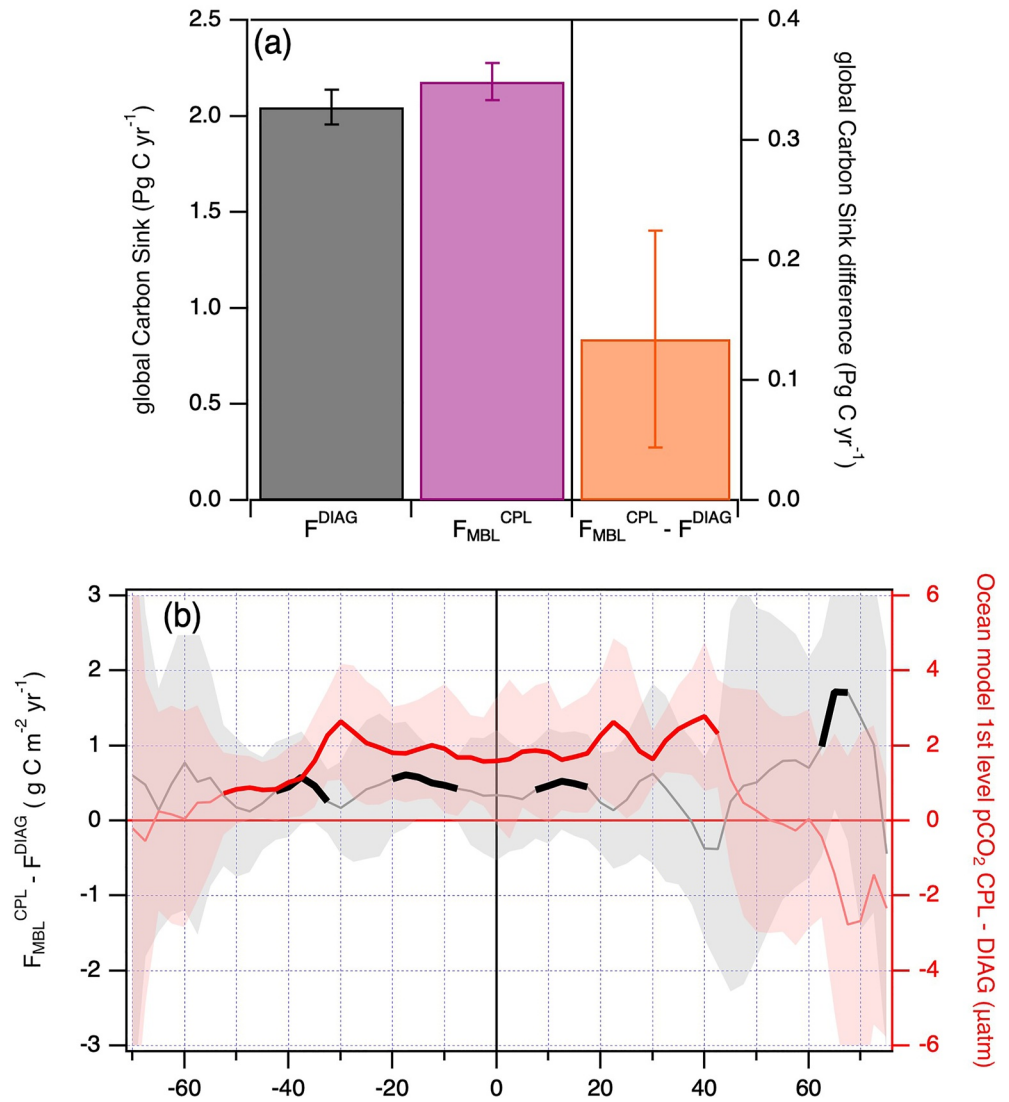
Figure 8. (a) Mean global carbon sink (PgC yr^{-1}) from DIAG and CPL simulations computed with F^{DIAG} (black bar, left axis) and F_{MBL}^{CPL} (purple bar, left axis), respectively; the difference is plotted in orange (right axis). Whiskers represent the year-to-year standard deviation. $F_{MBL}^{CPL} - F^{DIAG}$ is significantly different from zero at the 99% level. (b) The zonal and 15-year mean difference between F_{MBL}^{CPL} and F^{DIAG} (g C m^{-2} yr^{-1}, left axis) and the difference between the ocean model's first level pCO$_2$ between CPL and DIAG simulations (µatm, red, right axis). Shadings represent the year-to-year variability. Lines are bold where the difference is significantly different from zero at the 99% level.

the adjustment using a uniform ocean skin with the diagnostic flux F_{Wat}^{DIAG} (+0.33 PgC yr^{-1}) although weaker is not significantly different than the adjustment found by Watson et al. (2020, +0.4 ± 0.04 PgC yr^{-1}) and Dong et al. (2022, +0.39 ± 0.08 PgC yr^{-1}). The adjustment found with an interactive ocean skin and the rapid model with the diagnostic flux F_{TBL}^{DIAG} (+0.26 PgC yr^{-1}) is also on the same order of magnitude because part of this difference is due to unresolved warm layers (−0.02 PgC yr^{-1}) and salinity skin (−0.02 PgC yr^{-1}) effects that are not taken into account by previous studies. Surprisingly, whereas we find a significant sensitivity of the adjustment to considering an interactive ocean skin or not (F_{TBL}^{DIAG} vs. F_{Wat}^{DIAG}), Dong et al. (2022) and Watson et al. (2020) adjustments are very close to each other. This is partly explained by the fact that Dong et al. (2022) do not consider warm layer and salty skin corrections that would tend to reduce the adjustment. This may also arise from the use of monthly mean parameter in computing the adjustment.

4.2. Uncertainties Due To the Chemical Equilibrium

A second uncertainty comes from the chemical equilibrium assumption at the base of the MBL. The difference between the equilibrium model F_{MBL}^{DIAG} and the rapid model F_{TBL}^{DIAG} (+0.11 PgC yr^{-1}) is a measure of this uncertainty. As discussed by Dong et al. (2022) and Woolf et al. (2016), the residence time of a water parcel in the TBL is generally on the order of 1 s. This is shorter than the 10 s timescale of the chemical repartitioning of the carbonate species that is induced by changes in temperature and salinity. This is the reason why they recommend the rapid model that takes the temperature at the base of the TBL to represent the actual chemical repartitioning at the base of the MBL and compute $[CO_{2aq}]_w$ in Equation 2. However, they also note that the residence time of a water parcel can be longer under weak wind conditions: It can reach about 6 s for a 2 ms^{-1} wind speed (Garbe et al., 2004) and might even be longer due to the stabilizing effect of sunlight. These conditions are frequent in the tropics which may make the equilibrium hypothesis more suitable there. It is also where the difference between F_{MBL}^{DIAG} and F_{TBL}^{DIAG} adjustments is the largest (Figures 6b and 6c). The actual flux adjustment due to ocean skin is therefore certainly in between the results obtained for F_{MBL}^{DIAG} and F_{TBL}^{DIAG}. Refining the ocean skin parameterization to take into account the residence time of water parcel and the kinematics of the chemical repartitioning of the carbonate system could help reduce this uncertainty.

4.3. Cool Skin as a Function of Wind Speed Only

Because the cool skin mainly depends on the wind speed (Donlon et al., 2002), the use of a wind-only parameterization may appear sufficient to represent the cool skin effect in models. Figure 9a shows the mean temperature difference across the TBL computed by Bellenger et al. (2017) as a function of the model wind speed at 10 m. The large standard deviation in Figure 9 shows that the modeled cool skin does not only depend on wind speed but also on other factors such as air-sea gradients in temperature and humidity (e.g., Luo & Minnett, 2020). Figure 9b shows the mean annual difference between the cool skin temperature computed either by the Bellenger et al. (2017) parameterization or from the mean wind-only relationship shown in Figure 9a. A striking result is that large regions of negative and positive anomalies appear on this annual mean map (Figure 9b). Negative anomalies mean that the average cool skin is stronger than the one deduced from the wind-only relationship, and vice versa. In absolute value, these mean anomalies can be of the order of magnitude as the cool skin effect (~0.1 K, Figures 4a and 4b and 9b). If a mean wind dependency of the cool skin (Figure 9a) such as Donlon et al. (2002) is used to represent the cool skin effect in a model, it would lead to such regional biases in temperature at the interface and thus to regional errors in CO_2 fluxes of the order of magnitude discussed previously (Figures 6b and 6c).

4.4. Uncertainties Due to the CO_2 Transfer Velocity

This study is based on the assumption that the widely used bulk flux formulation of the transfer velocity k_w in Equation 2 that is derived from measurements in the bulk of water and air (see Wanninkhof et al., 2009 for a review) do not implicitly take into account the cool skin effect and can therefore be applied to study the impact of the ocean skin on the CO_2 flux. Dong et al. (2022) argued that global k_w based on ^{14}C inventory is not sensitive to the ocean skin correction due to the large air-sea ^{14}C difference. The same argument stands for in situ measurements based on $^3He/SF_6$ dual-tracers (e.g., Ho et al., 2006, Y. Dong personal communication). Therefore, the usual k_w formulation appears to be suitable to study the ocean skin effect as it has been implicitly hypothesized in previous studies (McGillis & Wanninkhof, 2006; Robertson & Watson, 1992; Watson et al., 2020; Woolf et al., 2016).

However, the bulk k_w accounts for a variety of processes such as exchanges mediated by bubbles, sea sprays and whitecaps associated with wave breaking. These processes become important for moderate winds (Fairall et al., 2000; Hare et al., 2004; Woolf et al., 2019). Because, these processes do not depend on the molecular microlayers, the use of a bulk transfer coefficient may lead to an overestimation of the associated CO_2 flux adjustment. In order to apply the ocean skin correction only to the part of the exchange mediated by the molecular sublayer, it seems suitable to treat separately the different CO_2 transfer processes.
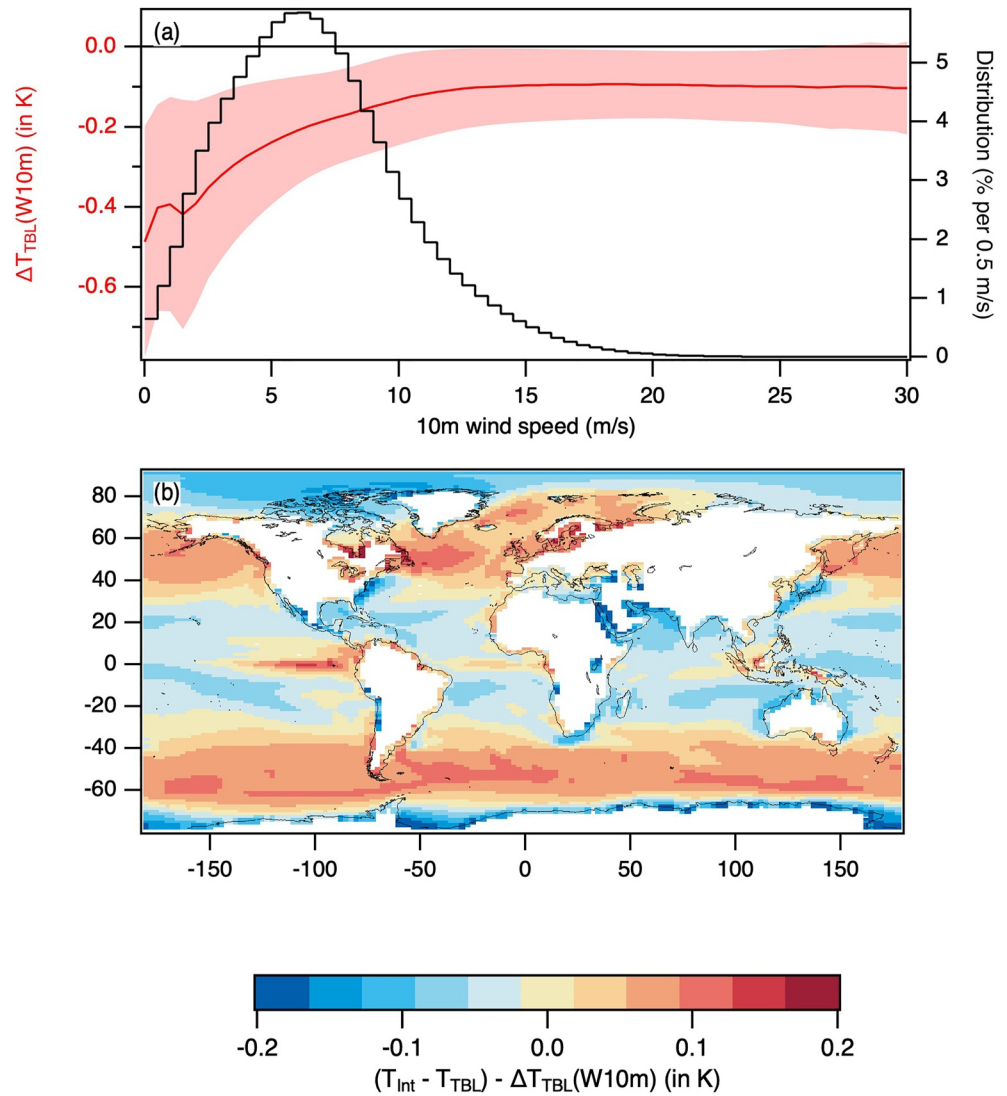
Figure 9. (a) Mean cool skin effect as a function of 10 m wind speed ($T_{Int} - T_{TBL} = \Delta T_{TBL}$(W10 m), red solid line) from IPSL-CM6 and associated standard deviation (red shading) and 10 m wind speed distribution per 0.1 m/s bin (black line). (b) 15-year mean difference (colors in K) between the cool skin effect from IPSL-CM6 and the cool skin effect computed from the mean relationship plotted in (a). The difference between the cool skins is computed using 90 min-model outputs and averaged over time.

5. Conclusions

This study explored the impact of thermal and saline gradients in the ocean skin on global atmosphere-ocean CO_2 fluxes. To achieve this, a global model with interactive temperature and salinity changes in the thermal and mass boundary layers (TBL and MBL) and the first layer of the ocean model (Bellenger et al., 2017) was used. These changes observed were dominated by temperature and salinity variations in their respective diffusive boundary layers, with an average increase in salinity of +0.06 g/kg and a decrease in temperature of −0.23 K. These results were consistent with those obtained by using ERA5 to force the parameterization of the ocean skin.

Using a bulk formulation of the CO_2 flux (McGillis & Wanninkhof, 2006; Woolf et al., 2016), several flux diagnostics are computed using temperature and salinity at different depths with or without (a) assuming the chemical equilibrium at the base of the MBL, (b) considering an interactive ocean skin, (c) taking into account unresolved gradients below the microlayer in the ocean model's first level, and (d) taking into account the salinity skin (Table 1). These diagnostics are consistent with previous studies (Dong et al., 2022; Shutler et al., 2020; Watson et al., 2020; Woolf et al., 2016, 2019). It was however possible to reveal the sensitivity of the adjustment

to these different assumptions: Depending on the assumption of whether the chemical equilibrium is reached at the base of the MBL (F_{MBL}) or not (F_{TBL}) leads to diagnostic global CO_2 sink adjustment of +0.37 and +0.26 Pg yr^{-1}, respectively. With a 1-m surface resolution ocean model, the unresolved warm layers and rain lenses only account for a reduction of the adjustment of −0.02 PgC yr^{-1}, comparable to the impact of the salty skin. Uniform ocean skin (F_{Wat}) lead to regional biases in the modeled CO_2 fluxes (+1 to +2 Pg C yr^{-1} in the Southern Ocean, Figure 6) and in the global sink (+0.33 against +0.26 Pg C yr^{-1}). This could impact the simulated carbon cycle and the representation of pathways of anthropogenic carbon, in particular, in the Southern Ocean where the vertical mixing induces large carbon subduction (e.g., Bopp et al., 2015). More importantly, ocean skin adjustment in a coupled model is weaker than diagnostic estimates. Indeed, we show that taking into account retroaction loops by enabling the ocean skin to feedback on ocean carbon concentrations dampens the magnitude of this adjustment to +0.13 (±0.09) PgC y^{-1}. Although significantly weaker than previous diagnostics, and although this adjustment obtained assuming the equilibrium model constitutes an upper limit, this remains a non-negligible impact on the global ocean carbon sink (on the order of 5%) with regional signature and it is linked to a change of the modeled mean surface pCO_2. The magnitude of these changes ultimately depends on the capacity of the ocean model to transfer CO_2 in its interior.

Future modeling efforts should thus take into account the ocean skin impact on CO_2 flux. An interactive parameterization of the ocean skin appears to be necessary to prevent regional errors in CO_2 flux. As a next step, a detailed flux parameterization (e.g., Fairall et al., 2000) should be tested in climate models because the ocean skin adjustment would be only applied to the exchanges mediated by the molecular microlayer. This should further reduce the impact of the ocean skin on the modeled CO_2 sink. Note that this effort to separate the different process, that are not all sensitive to the ocean skin, seems also important for observation assessments of global CO_2 sink. This may as well reduce the diagnosed impact of ocean skin on the global sink compared to previous estimates (Dong et al., 2022; Watson et al., 2020). On the other hand, taking into account the kinematics of chemical repartitioning of the carbonate species with temperature and salinity (Woolf et al., 2016) could increase the ocean skin effect in the tropics and thus the adjustment of the global sink.

Appendix A: Sensitivity of CO_2 Flux to Ocean Near-Surface Temperature and Salinity Changes

We derive an approximate formula for the change in carbon flux due to perturbations in temperature and salinity near the ocean surface. This will provide a synthesis of the different sensitivities of the main terms of Equation 2 to T and S discussed in Woolf et al. (2016) and their order of magnitudes. In the following, we assume that the aqueous carbonate system is in chemical equilibrium for a given environment (i.e., for given T, S, DIC, and Alk).

Neglecting the sensitivity of the Schmidt number on temperature for changes of at most a few degrees that are considered here, and supposing no change in the wind, the total derivative of the flux reads:

$$dF = k_w \sqrt{660/\text{Sc}(T)} \big[d\left[\text{CO}_{2aq}\right]_i (T, S) - d\left[\text{CO}_{2aq}\right]_w (T, S, \text{DIC}, \text{Alk})\big] \tag{A1}$$

The total derivative of $[\text{CO}_{2aq}]_i$ can be directly derived using formula from Weiss (1974) and provided by McGillis and Wanninkhof (2006). The total derivative for $[\text{CO}_{2aq}]_w$, which reflects a change in aqueous CO_2 due to chemical processes, reads:

$$d\left[\text{CO}_{2aq}\right]_w = dT \frac{\partial\left[\text{CO}_{2aq}\right]_w}{\partial T} + dS \frac{\partial\left[\text{CO}_{2aq}\right]_w}{\partial S} + d\text{Alk} \frac{\partial\left[\text{CO}_{2aq}\right]_w}{\partial Alk} + d\text{DIC} \frac{\partial\left[\text{CO}_{2aq}\right]_w}{\partial \text{DIC}} \tag{A2}$$

We make the hypothesis that near the surface, Alk and DIC only change by dilution:

$$d\text{Alk} \frac{\partial\left[CO_{2aq}\right]_w}{\partial Alk} = Alk \frac{dS}{S} \frac{\partial\left[CO_{2aq}\right]_w}{\partial Alk} \tag{A3}$$

Noting that the solubility K_0 is not a function of Alk and DIC and introducing γ_{Alk} and γ_{DIC} the sensitivity of pCO_{2w} to Alk and DIC, the two last terms in Equation A2 can be written:

$$d\text{Alk} \frac{\partial\left[CO_{2aq}\right]_w}{\partial Alk} + d\text{DIC} \frac{\partial\left[CO_{2aq}\right]_w}{\partial DIC} = dS\left(K_0 \frac{\text{pCO}_{2w}}{S}\gamma_{Alk} + K_0 \frac{\text{pCO}_{2w}}{S}\gamma_{DIC}\right) \tag{A4}$$

Using approximations in Sarmiento and Gruber (2006), it comes that $\gamma_{Alk} + \gamma_{DIC} = 1$ and thus substituting Equation A4 in Equation A2 leads to:

$$d\left[CO_{2aq}\right]_w = dT \frac{\partial\left[CO_{2aq}\right]_w}{\partial T} + \left(\frac{\partial\left[CO_{2aq}\right]_w}{\partial S} + K_0.\frac{pCO_{2w}}{S}\right)dS \qquad (A5)$$

Using the relationship of pCO_{2w} mean sensitivity to temperature and salinity given by Takahashi et al. (2009) leads to:

$$d\left[CO_{2aq}\right]_w = \left(\frac{\partial K_0}{\partial T} + \gamma_T K_0\right)pCO_{2w}\,dT + \left(\frac{\partial K_0}{\partial S} + \frac{2K_0}{S}\right)pCO_{2w}\,dS \qquad (A6)$$

This last equation enables to make a simple estimate of the sensitivities of $[CO_{2aq}]_w$ to changes in temperature (dT) and salinity (dS) for given values of T, S and pCO_{2w}.

In order to illustrate the validity of our approximation to represent changes in the water-side CO_2 concentration near the surface, we show on Figure A1 a scatterplot of the $d[CO_{2aq}]_w$ approximated from Equation A6 and computed using $dT = T_{int} - T_{h/2}$ and $dS = S_{int} - S_{h/2}$ as a function of $d\left[CO_{2aq}\right]_{w=}\left[CO_{2aq}\right]_w(T_{int}, S_{int}, DIC_{int}, Alk_{int}) - \left[CO_{2aq}\right]_w\left(T_{h/2}, S_{h/2}, DIC_{h/2}, Alk_{h/2}\right)$ computed by the IPSL-CM6 model following MOCSY set of equations (Orr & Epitalon, 2015). Note that we compute the difference to a hypothetical interfacial $[CO_{2aq}]_w$ in order to have larger differences in T and S (see Figure 3). Although slightly overestimating the change in $[CO_{2aq}]_w$, (Equation A6) is a good approximation where the sea temperature is above 0°C (and even better in relatively warm waters).
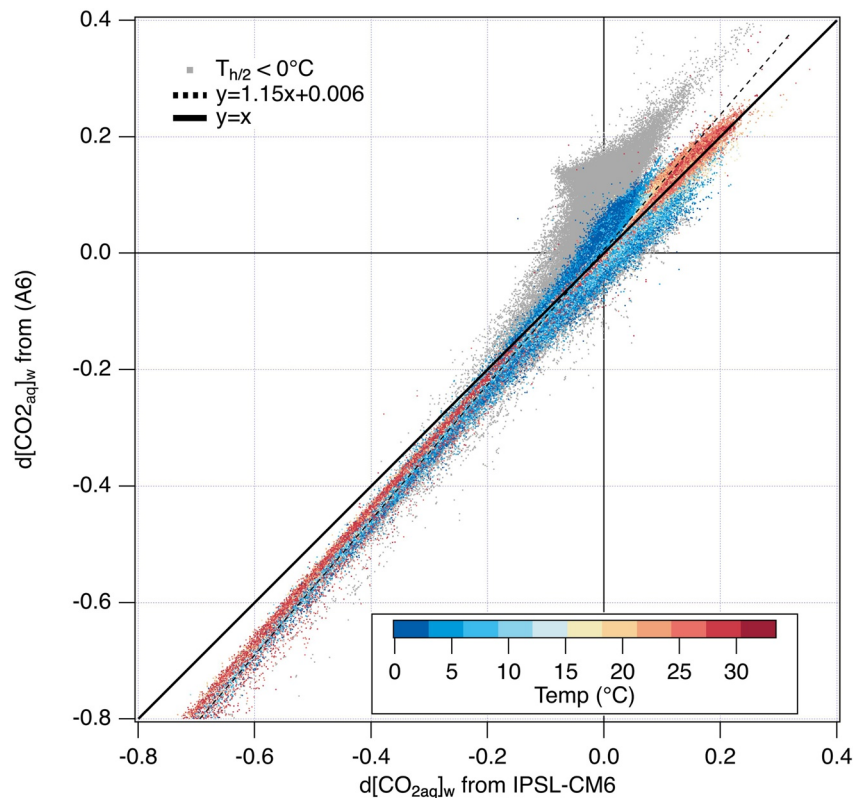

Figure A1. Differences in the aqueous carbon concentration $[CO_{2aq}]_w$ in mmol m^{-3} between the interface and $h/2$ approximated from Equation A6 using $dT = T_{int} - T_{h/2}$ and $dS = S_{int} - S_{h/2}$ and IPSL-CM6 outputs ($d[CO_{2aq}]_w$ approx.) and directly calculated by IPSL-CM6 ($d[CO_{2aq}]_w$ IPSL-CM6). Color is the ocean model first level temperature (gray dots for temperatures below 0°C). The linear fit is also plotted.
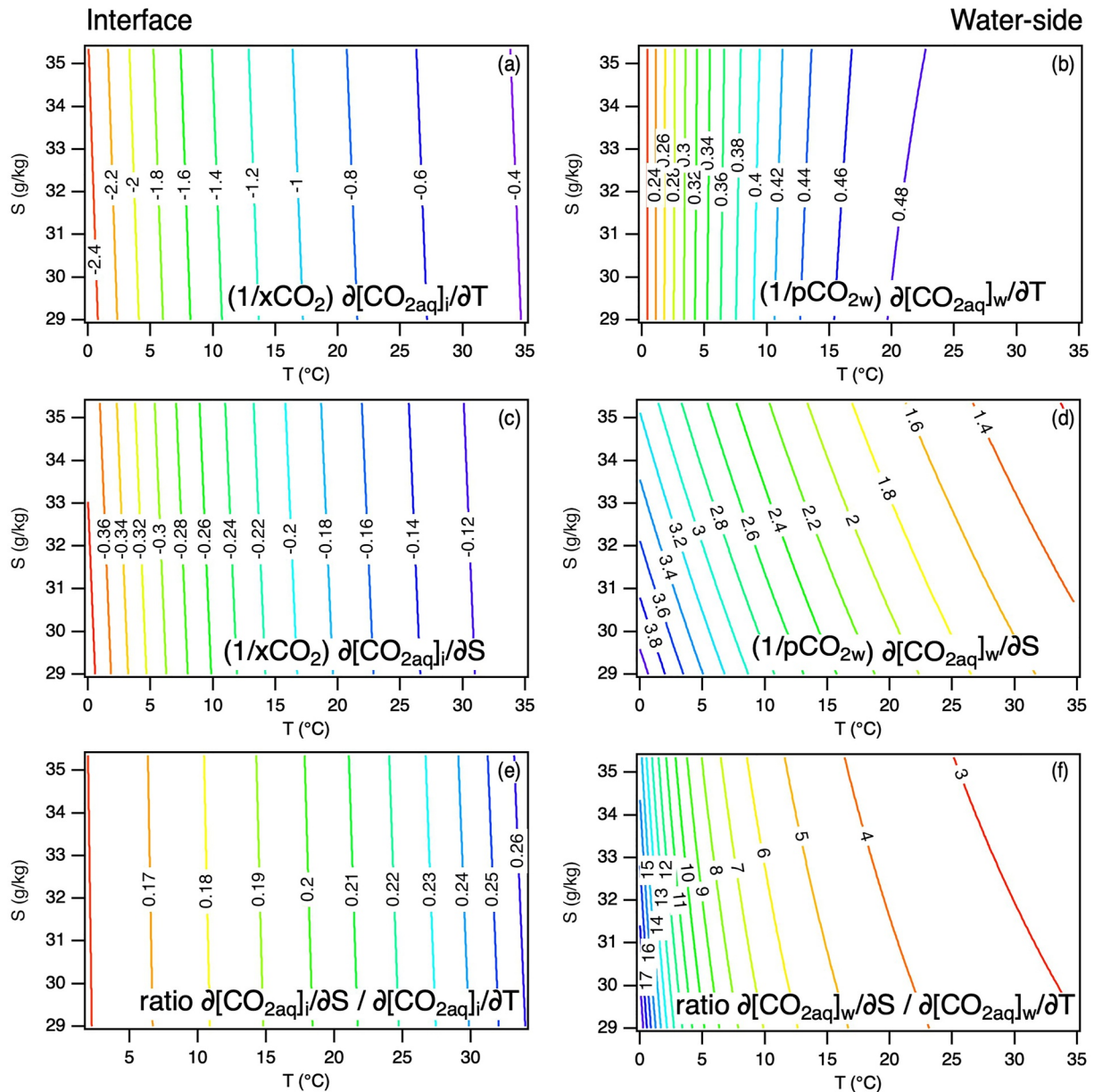
Figure A2. Sensitivity of the interfacial carbon concentration $[CO_{2aq}]_i$ divided by the atmospheric concentration of CO_2 (xCO_2, (a and c)) and the aqueous carbon concentration $[CO_{2aq}]_w$ divided by the CO_2 partial pressure in water (pCO_{2w}, (b) and (d)) to temperature (a and b) and salinity (c and d) and the ratio of these sensitivities for (e) $[CO_{2aq}]_i$ and (f) $[CO_{2aq}]_w$ as a function of temperature and salinity. The sensitivities of $[CO_{2aq}]_i$ and $[CO_{2aq}]_w$ to T ad S are respectively in mol m^{-3} atm^{-1} K^{-1} and mol m^{-3} atm^{-1} (g/kg)$^{-1}$, pCO_{2w} in atm and xCO_2 the atmospheric CO_2 mole fraction in mol/mol. The sensitivities of $[CO_{2aq}]_i$ are from Weiss formulation and the sensitivities of $[CO_{2aq}]_w$ are computed from Equation A6.

Figure A2 shows the sensitivity of $[CO_{2aq}]_i$ and $[CO_{2aq}]_w$ to Temperature and Salinity (respectively divided by the atmospheric CO_2 mole fraction and pCO_{2w}) and their ratio. The interface concentration $[CO_{2aq}]_i$ is a decreasing function of both temperature and salinity (Figures A2a and A2c). Its temperature sensitivity is 4–6 times larger than to salinity (Figure A2e). This means that an increase of 0.6 g/kg in S_{Int} is needed to offset a decrease of −0.1 K in T_{Int}. This is rarely the case, so usually the dominating effect is an increase of $[CO_{2aq}]_i$ due to the cool skin. On the other hand, $[CO_{2aq}]_w$ is an increasing function of temperature and salinity (Figures A2b and A2d). Its sensitivity to salinity is 3–10 times larger than its sensitivity to temperature (Figures A2f). This ratio increases up to 17 with decreasing temperature to 0°C, but our approximation does not hold in cold Polar regions (Figure A1). If $[CO_{2aq}]_w$ is evaluated at the base of the MBL (in F_{MBL}), the variations in T and S that can

influence it are changes below the TBL and MBL ($T_{TBL} − T_d$ and $S_{MBL} − S_d$) and changes in the cool skin below the MBL ($T_{TBL} − T_{MBL}$). The former is due to diurnal warm layer formation or rain-induced freshening and cooling. Because these differences are usually weak in our simulations (Figure 3) they only affect $[CO_{2aq}]_w$ locally. The latter corresponds in our simulations to 4/5th of $T_{int} − T_{TBL}$, the entire cool skin effect, and induces a decrease in $[CO_{2aq}]_w$. Finally, an increase in $[CO_{2aq}]_i$ and a decrease in $[CO_{2aq}]_w$ together induce the obtained increase in the global carbon sink (Figure 5a, the red bar). For F_{TBL}, the main impact (except for warm layers and rain lenses) is the increase in $[CO_{2aq}]_i$ with decreasing T.

Note that, considering only the impact of temperature on CO_2 flux (Equation A1) leads to:

$$F_{MBL} − F = k_w \sqrt{660/Sc(T)} \left[(T_{Int} − T_{h/2}) \frac{\partial [CO_{2aq}]_i}{\partial T} − (T_{MBL} − T_{h/2}) \frac{\partial [CO_{2aq}]_w}{\partial T} \right] \quad (A7)$$

That can be rearranged to

$$F_{MBL} − F = k_w \sqrt{660/Sc(T)} \left[(T_{Int} − T_{h/2}) \left(\frac{\partial [CO_{2aq}]_i}{\partial T} − \frac{\partial [CO_{2aq}]_w}{\partial T} \right) + (T_{Int} − T_{MBL}) \frac{\partial [CO_{2aq}]_w}{\partial T} \right] \quad (A8)$$

The first term in the parenthesis is positive, the second is negative. Therefore, the flux adjustment due to F_{MBL} increase when T_{MBL} tends to T_{int} (or if the MBL becomes thinner). Therefore, unlike discussed in McGillis and Wanninkhof (2006) and as discussed by Woolf et al. (2016), a thinner MBL would lead to a stronger F_{MBL} flux adjustment with a maximum value given by the total temperature difference in the ocean skin ($T_{int} − T_{h/2}$) that is reached for $T_{MBL} = T_{int}$.

Data Availability Statement

The ocean skin parameterization (Bellenger et al., 2017) is open-access and can be downloaded at https://gitlab.in2p3.fr/ipsl/lmd/dpao/ocean-skin. The CMIP6 historical simulations with IPSL-CM6A-LR (and in particular the r1i1p1f1 member) are available on ESGF: https://esgf-node.ipsl.upmc.fr/search/cmip6-ipsl/. Surface ERA5 hourly data can be accessed from https://cds.climate.copernicus.eu/cdsapp#!/dataset/reanalysis-era5-single-levels?tab=overview. Daily CO_2 fluxes from DIAG ad CPL simulations and temperature and salinity changes in the ocean skin from DIAG can be found https://zenodo.org/record/7731926.

References

Aumont, O., Ethé, C., Tagliabue, A., Bopp, L., & Gehlen, M. (2015). PISCES-v2: An ocean biogeochemical model for carbon and ecosystem studies. *Geoscientific Model Development*, 8, 2465–2513. https://doi.org/10.5194/gmd-8-2465-2015

Bakker, D. C., Pfeil, B., Landa, C. S., Metzl, N., O'Brien, K. M., Olsen, A., et al. (2016). A multi-decade record of high-quality fCO₂ data in version 3 of the Surface Ocean CO₂ Atlas (SOCAT). *Earth System Science Data*, 8(2), 383–413. https://doi.org/10.5194/essd-8-383-2016

Banzon, V., Smith, T. M., Chin, T. M., Liu, C., & Hankins, W. (2016). A long-term record of blended satellite and in situ sea-surface temperature for climate monitoring, modeling and environmental studies. *Earth System Science Data*, 8(1), 165–176. https://doi.org/10.5194/essd-8-165-2016

Bellenger, H., Drushka, K., Asher, W. E., Reverdin, G., Katsumata, M., & Watanabe, M. (2017). Extension of the prognostic model of sea surface temperature to rain-induced cool and fresh lenses. *Journal of Geophysical Research: Oceans*, 122(1), 484–507. https://doi.org/10.1002/2016JC012429

Bellenger, H., & Duvel, J. P. (2009). An analysis of ocean diurnal warm layers over tropical oceans. *Journal of Climate*, 22(13), 3629–3646. https://doi.org/10.1175/2008jcli2598.1

Bolin, B. (1960). On the exchange of carbon dioxide between the atmosphere and the sea. *Tellus*, 12(3), 274–281. https://doi.org/10.3402/tellusa.v12i3.9402

Bopp, L., Levy, M., Resplandy, L., & Sallée, J. B. (2015). Pathways of anthropogenic carbon subduction in the global ocean. *Geophysical Research Letters*, 42(15), 6416–6423. https://doi.org/10.1002/2015GL065073

Boucher, O., & coauthors (2020). Presentation and evaluation of the IPSL-CM6A-LR climate model. *Journal of Advances in Modeling Earth System*, 12, e2019MS002010. https://doi.org/10.1029/2019MS002010

Dong, Y., Bakker, D. C. E., Bell, T. G., Huang, B., Landschützer, P., Liss, P., & Yang, M. (2022). Update on the temperature corrections of global air-sea CO₂ flux estimate. *Global Biogeochemical Cycles*, 36(9). e2022GB007360. https://doi.org/10.1029/2022GB007360

Dong, Y., Yang, M., Bakker, D. C. E., Liss, P. S., Kitidis, V., Brown, I., et al. (2021). Near-surface stratification due to ice melt biases Arctic air-sea CO₂ flux estimates. *Geophysical Research Letters*, 48(22), 1–10. https://doi.org/10.1029/2021GL095266

Donlon, C. J., Minnett, P. J., Gentemann, C., Nightingale, T. J., Barton, I. J., Ward, B., & Murray, M. J. (2002). Toward improved validation of satellite sea surface skin temperature measurements for climate research. *Journal of Climate*, 15(4), 353–369. https://doi.org/10.1175/1520-0442(2002)015<0353:tivoss>2.0.co;2

Drushka, K., Asher, W. E., Ward, B., & Walesby, K. (2016). Understanding the formation and evolution of rain-formed fresh lenses at the ocean surface. *Journal of Geophysical Research: Oceans*, *121*(4), 2673–2689. https://doi.org/10.1002/2015JC011527

Fairall, C. W., Bradley, E. F., Godfrey, J. S., Wick, G. A., Edson, J. B., & Young, G. S. (1996). Cool-skin and warm-layer effects on sea surface temperature. *Journal of Geophysical Research*, *101*(C1), 1295–1308. https://doi.org/10.1029/95JC03190

Fairall, C. W., Hare, J. E., Edson, J. B., & McGillis, W. (2000). Parameterization and micrometeorological measurement of air-sea gas transfer. *Boundary Layer Met*, *96*, 63–105.

Fay, A. R., Gregor, L., Landschützer, P., McKinley, G. A., Gruber, N., Gehlen, M., et al. (2021). SeaFlux: Harmonization of air–sea CO_2 fluxes from surface pCO_2 data products using a standardized approach. *Earth System Science Data*, *13*(10), 4693–4710. https://doi.org/10.5194/essd-13-4693-2021

Friedlingstein, P., Jones, M. W., O'Sullivan, M., Andrew, R. M., Bakker, D. C. E., Hauck, J., et al. (2022). Global carbon budget 2021 Earth system. *Science Data*, *14*(4), 1917–2005. https://doi.org/10.5194/essd-14-1917-2022

Garbe, C. S., Schimpf, U., & Jähne, B. (2004). A surface renewal model to analyse infrared image sequences of the ocean surface for the study of air-sea heat and gas exchange. *Journal of Geophysical Research*, *109*(C8), C08S15. https://doi.org/10.1029/2003JC001802

Gruber, N., Clement, D., Carter, B. R., Feely, R. A., van Heuven, S., Hoppema, M., et al. (2019). The oceanic sink for anthropogenic CO_2 from 1994 to 2007. *Science*, *363*(6432), 1193–1199. https://doi.org/10.1126/science.aau5153

Hare, J. E., Fairall, C. W., McGillis, W. R., Edson, J. B., Ward, B., & Wanninkhof, R. (2004). Evaluation of the National Oceanic and Atmospheric Administration/Coupled-Ocean Atmospheric Response Experiment (NOAA/COARE) air-sea gas transfer parameterization using GasEx data. *Journal of Geophysical Research*, *109*(C8), C08S11. https://doi.org/10.1029/2003JC001831

Hersbach, H., Bell, B., Berrisford, P., Hirahara, S., Horányi, A., Muñoz-Sabater, J., et al. (2020). The ERA5 global reanalysis. *Quarterly Journal of the Royal Meteorological Society*, *146*(730), 1999–2049. https://doi.org/10.1002/qj.3803

Ho, D. T., Bliven, L. F., Wanninkhof, R., & Schlosser, P. (1997). The effect of rain on air-water gas exchange. *Tellus*, *49*(2), 149–158. https://doi.org/10.3402/tellusb.v49i2.15957

Ho, D. T., Law, C. S., Smith, M. J., Schlosser, P., Harvey, M., & Hill, P. (2006). Measurements of air-sea gas exchange at high wind speeds in the Southern Ocean: Implications for global parameterization. *Geophysical Research Letters*, *33*(16), L16611. https://doi.org/10.1029/2006GL026817

Ho, D. T., & Schanze, J. J. (2020). Precipitation-induced reduction in surface ocean pCO_2: Observations from the eastern Tropical Pacific Ocean. *Geophysical Research Letters*, *47*(15). e2020GL088252. https://doi.org/10.1029/2020GL088252

Hourdin, F., Rio, C., Grandpeix, J.-Y., Madeleine, J.-B., Cheruy, F., Rochetin, N., et al. (2019). LMDZ6: The improved atmospheric component of the IPSL coupled model. *Journal of Advances in Modeling Earth Systems*, 2019MS001988. https://doi.org/10.1029/2019MS001892

Katsaros, K., & Buettner, K. J. K. (1969). Influence of rainfall on temperature and salinity of the ocean surface. *Journal of Applied Meteorology*, *8*(1), 15–18. https://doi.org/10.1175/1520-0450(1969)008<0015:iorota>2.0.co;2

Kawai, Y., & Wada, A. (2007). Diurnal sea surface temperature variation and its impact on the atmosphere and ocean: A review. *Journal of Oceanography*, *63*(5), 721–744. https://doi.org/10.1007/s10872-007-0063-0

Large, W. G., McWilliams, J. C., & Doney, S. C. (1994). Oceanic vertical mixing: A review and a model with a nonlocal boundary layer parameterization. *Review of Geophysics*, *32*(4), 363–403. https://doi.org/10.1029/94rg01872

Lengaigne, M., Madec, G., Bopp, L., Menkes, C., Aumont, O., & Cadule, P. (2009). Bio-physical feedbacks in the Arctic Ocean using an Earth system model. *Geophysical Research Letters*, *36*(21), L21602. https://doi.org/10.1029/2009GL040145

Liss, P. S., & Slater, P. G. (1974). Flux of gases across the air-sea interface. *Nature*, *274*(5438), 181–184. https://doi.org/10.1038/247181a0

Luo, B., & Minnett, P. J. (2020). Evaluation of the ERA5 Sea Surface Skin Temperature with remotely sensed shipborne marine atmospheric emitted radiance interferometer data. *Remote Sensing*, *12*(11), 1873. https://doi.org/10.3390/rs12111873

Madec, G., Bourdalle-Badie, R., Bouttier, P., Bricaud, C., Bruciaferri, D., Calvert, D., & Vancoppenolle, M. (2017). *NEMO ocean engine (version v3.6)*. Notes du Pôle de modelisation de l'Institut Pierre-Simon Laplace (IPSL). https://doi.org/10.5281/zenodo.1472492

McGillis, W. R., & Wanninkhof, R. (2006). Aqueous CO_2 gradients for air-sea flux estimates. *Marine Chemistry*, *98*(1), 100–108. https://doi.org/10.1016/j.marchem.2005.09.003

Merchant, C. J., Embury, O., Bulgin, C. E., Block, T., Corlett, G. K., Fiedler, E., et al. (2019). Satellite-based time-series of sea-surface temperature since 1981 for climate applications. *Scientific Data*, *6*(1), 1–18. https://doi.org/10.1038/s41597-019-0236-x

Miller, L. A., Burgers, T. M., Burt, W. J., Granskog, M. A., & Papakyriakou, T. N. (2019). Air-Sea CO_2 flux estimates in stratified Arctic coastal waters: How wrong can we be? *Geophysical Research Letters*, *46*(1), 235–243. https://doi.org/10.1029/2018GL080099

Moulin, A. J., Moum, J. N., Shroyer, E. L., & Hoecker-Martinez, M. (2021). Freshwater lens fronts propagating as buoyant gravity currents in the equatorial Indian Ocean. *Journal of Geophysical Research: Oceans*, *126*(8), e2021JC017186. https://doi.org/10.1029/2021JC017186

Olivier, L., Boutin, J., Reverdin, G., Lefèvre, N., Landschützer, P., Speich, S., et al. (2022). Wintertime process study of the North Brazil Current rings reveals the region as a larger sink for CO_2 than expected. *Biogeosciences*, *19*(12), 2969–2988. https://doi.org/10.5194/bg-19-2969-2022

Orr, J. C., & Epitalon, J.-M. (2015). Improved routines to model the ocean carbonate system: Mocsy 2.0. *Geoscientific Model Development*, *8*(3), 485–499. https://doi.org/10.5194/gmd-8-485-2015

Regnier, P., Resplandy, L., Najjar, R. G., & Ciais, P. (2022). The land-to-ocean loops of the global carbon cycle. *Nature*, *603*(7901), 401–410. https://doi.org/10.1038/s41586-021-04339-9

Reverdin, G., Morisset, S., Boutin, J., & Martin, N. (2012). Rain-induced variability of near sea-surface T and S from drifter data. *Journal of Geophysical Research*, *117*(C2), C02032. https://doi.org/10.1029/2011JC007549

Reverdin, G., Supply, A., Drushka, K., Thompson, E. J., Asher, W. E., & Lourenço, A. (2020). Intense and small freshwater pools from rainfall investigated during SPURS-2 on 9 November 2017 in the Eastern Tropical Pacific. *Journal of Geophysical Research: Oceans*, *125*(2), e2019JC015558. https://doi.org/10.1029/2019JC015558

Robertson, J. E., & Watson, A. J. (1992). Thermal skin effect of the surface ocean and its implications for CO_2 uptake. *Nature*, *358*(6389), 738–740. https://doi.org/10.1038/358738a0

Sarmiento, J. L., & Gruber, N. (2006). *Ocean biogeochemical Dynamics* (Vol. xiii, p. 503). Princeton University Press.

Saunders, P. M. (1967). The temperature at the ocean–air interface. *Journal of the Atmospheric Sciences*, *24*(3), 269–273. https://doi.org/10.1175/1520-0469(1967)024<0269:ttatoa>2.0.co;2

Schlussel, P., Soloviev, A. V., & Emery, W. J. (1997). Cool and freshwater skin of the ocean during rainfall. *Boundary-Layer Meteorology*, *82*, 437–472.

Shutler, J. D., Wanninkhof, R., Nightingale, P. D., Woolf, D. K., Bakker, D. C. E., Watson, A., et al. (2020). Satellites will address critical science priorities for quantifying ocean carbon. *Frontiers in Ecology and the Environment*, *18*(1), 27–35. https://doi.org/10.1002/fee.2129

Soloviev, A., & Lukas, R. (2014). *The near-surface layer of the Ocean: Structure, dynamics and applications* (p. 572). Springer. https://doi.org/10.1007/978-94-007-7621-0

Stommel, H., Saunders, K., Simmons, W., & Cooper, J. (1969). Observations of the diurnal thermocline. *Deep-Sea Research*, *16*(suppl), 269–284.

Stuart-Menteth, A. C., Robinson, I. S., & Challenor, P. G. (2003). A global study of diurnal warming using satellite-derived sea surface temperature. *Journal of Geophysical Research*, *108*(C5), 3155. https://doi.org/10.1029/2002JC001534

Supply, A., Boutin, J., Reverdin, G., Vergely, J. L., & Bellenger, H. (2020). Variability of satellite sea surface salinity under rainfall. In V. Levizzani, C. Kidd, D. Kirschbaum, C. Kummerow, K. Nakamura, & F. Turk (Eds.), *Satellite precipitation measurement, Advances in global change research* (Vol. 69). Springer. https://doi.org/10.1007/978-3-030-35798-6_34

Takahashi, T., Sutherland, S. C., Wanninkhof, R., Sweeney, C., Feely, R. A., Chipman, D. W., et al. (2009). Climatological mean and decadal change in surface ocean pCO_2, and net sea-air CO_2 flux over the global oceans. *Deep Sea Research Part II: Topical Studies in Oceanography*, *56*(8–10), 554–577. https://doi.org/10.1016/J.DSR2.2008.12.009

Ten Doeschate, A., Sutherland, G., Bellenger, H., Landwehr, S., Esters, L., & Ward, B. (2019). Upper ocean response to rain observed from a vertical profiler. *Journal of Geophysical Research: Oceans*, *124*(6), 3664–3681. Wiley-Blackwell. https://doi.org/10.1029/2018jc014060

Turk, D., Zappa, C. J., Meinen, C. S., Christian, J. R., Ho, D. T., Dickson, A. G., & McGillis, W. R. (2010). Rain impacts on CO_2 exchange in the Western equatorial Pacific Ocean. *Geophysical Research Letters*, *37*(23), L23610. https://doi.org/10.1029/2010gl045520

Van Scoy, K. A., Morris, K. P., Robertson, J. E., & Watson, A. J. (1995). Thermal skin effect and the air-sea flux of carbon dioxide: A seasonal high-resolution estimate. *Global Biogeochemical Cycles*, *9*(2), 253–262. https://doi.org/10.1029/94GB03356

Walker Brown, C., Boutin, J., & Merlivat, L. (2015). New insights into fCO_2 variability in the tropical eastern Pacific Ocean using SMOS SSS. *Biogeosciences*, *12*(23), 7315–7329. https://doi.org/10.5194/bg-12-7315-2015

Wanninkhof, R. (2014). Relationship between wind speed and gas exchange over the ocean revisited. *Limnology and Oceanography: Methods*, *12*(6), 351–362. https://doi.org/10.4319/lom.2014.12.351

Wanninkhof, R., Asher, W. E., Ho, D. T., Sweeney, C., & McGillis, W. R. (2009). Advances in quantifying air-sea gas exchange and environmental forcing. *Annual Review of Marine Science*, *1*(1), 213–244. https://doi.org/10.1146/annurev.marine.010908.163742

Ward, B., Wanninkhof, R., McGillis, W. R., Jessup, A. T., DeGrandpre, M. D., Hare, J. E., & Edson, J. B. (2004). Biases in the air-sea flux of CO_2 resulting from ocean surface temperature gradients. *Journal of Geophysical Research*, *109*(C8), C08S08. https://doi.org/10.1029/2003JC001800

Watson, A. J., Schuster, U., Shutler, J. D., Holding, T., Ashton, I. G. C., Landschützer, P., et al. (2020). Revised estimates of ocean-atmosphere CO_2 flux are consistent with carbon inventory. *Nature Communications*, *11*(1), 4422. https://doi.org/10.1038/s41467-020-18203-3

Weiss, R. F. (1974). Carbon dioxide in water and seawater: The solubility of a non-ideal gas. *Marine Chemistry*, *2*(3), 203–215. https://doi.org/10.1016/0304-4203(74)90015-2

Woods, S., Minnett, P. J., Gentemann, C. L., & Bogucki, D. (2014). Influence of the oceanic cool skin layer on global air–sea CO_2 flux estimates. *Remote Sensing of Environment*, *145*, 15–24. https://doi.org/10.1016/j.rse.2013.11.023

Woolf, D. K., Land, P. E., Shutler, J. D., Goddijn-Murphy, L. M., & Donlon, C. J. (2016). On the calculation of air-sea fluxes of CO_2 in the presence of temperature and salinity gradients. *Journal of Geophysical Research: Oceans*, *121*(2), 1229–1248. https://doi.org/10.1002/2015jc011427

Woolf, D. K., Shutler, J. D., Goddijn-Murphy, L., Watson, A. J., Chapron, B., Nightingale, P. D., et al. (2019). Key uncertainties in the recent air-sea flux of CO_2. *Global Biogeochemical Cycles*, *33*(12), 1548–1563. https://doi.org/10.1029/2018GB006041

Yang, M., Bell, T. G., Bidlot, J. R., Blomquist, B. W., Butterworth, B. J., Dong, Y., et al. (2022). Global synthesis of air-sea CO_2 transfer velocity estimates from ship-based Eddy covariance measurements. *Frontiers in Marine Science*, *9*(June), 1–15. https://doi.org/10.3389/fmars.2022.826421

Yu, L. (2010). On sea surface salinity skin effect induced by evaporation and implications for remote sensing of ocean salinity. *Journal of Physical Oceanography*, *40*(1), 85–102. https://doi.org/10.1175/2009JPO4168.1

Zeng, X., & Beljaars, A. (2005). A prognostic scheme of sea surface skin temperature for modeling and data assimilation. *Geophysical Research Letters*, *32*(14), L14605. https://doi.org/10.1029/2005gl023030

Zhang, X., & Cai, W.-J. (2007). On some biases of estimating the global distribution of air-sea CO_2 flux by bulk parameterization. *Geophysical Research Letters*, *34*(1), L01608. https://doi.org/10.1029/2006GL027337

Zhang, Y., & Zhang, X. (2012). Ocean haline skin layer and turbulent surface convections. *Journal of Geophysical Research*, *117*(C4), C04017. https://doi.org/10.1029/s2011JC007464